



HAL
open science

An experimentally-determined general formalism for evaporation and isotope fractionation of Cu and Zn from silicate melts between 1300 and 1500 °C and 1 bar

Paolo Sossi, Frederic Moynier, Robin Treilles, Marwane Mokhtari, Xiang Wang, Julien Siebert

► To cite this version:

Paolo Sossi, Frederic Moynier, Robin Treilles, Marwane Mokhtari, Xiang Wang, et al.. An experimentally-determined general formalism for evaporation and isotope fractionation of Cu and Zn from silicate melts between 1300 and 1500 °C and 1 bar. *Geochimica et Cosmochimica Acta*, 2020, 10.1016/j.gca.2020.08.011 . hal-03021529

HAL Id: hal-03021529

<https://enpc.hal.science/hal-03021529>

Submitted on 9 Sep 2022

HAL is a multi-disciplinary open access archive for the deposit and dissemination of scientific research documents, whether they are published or not. The documents may come from teaching and research institutions in France or abroad, or from public or private research centers.

L'archive ouverte pluridisciplinaire **HAL**, est destinée au dépôt et à la diffusion de documents scientifiques de niveau recherche, publiés ou non, émanant des établissements d'enseignement et de recherche français ou étrangers, des laboratoires publics ou privés.



Distributed under a Creative Commons Attribution - NonCommercial 4.0 International License

1 **An experimentally-determined general formalism for evaporation and isotope fractionation of**
2 **Cu and Zn from silicate melts between 1300 - 1500 °C and 1 bar**

3 Paolo A. Sossi^{1,2*}, Frédéric Moynier¹, Robin Treilles¹, Marwane Mokhtari¹, Xiang Wang¹, Julien
4 Siebert¹

5 ¹ Institut de Physique du Globe de Paris, 1 rue Jussieu, F-75005, Paris, France

6 ² Institute of Geochemistry and Petrology, ETH Zürich, Sonneggstrasse 5, CH-8092, Zürich, Switzerland

7 * corresponding author. E-mail: paolo.sossi@erdw.ethz.ch

8 **Abstract**

9 Vapourisation fractionates elements and their isotopes between condensed phase(s) and the gas phase
10 according to two end-member regimes; kinetic (Langmuir) or equilibrium (Knudsen). The fractionation
11 factor of isotopes *i* and *j* of element E between gas and liquid, $^{ij}E(\alpha_{vap-liq})$, in the former case depends
12 only on the molar masses of the evaporating species, $(M_j/M_i)^{0.5}$, whereas, at equilibrium, fractionation
13 is ~ 1 at high temperatures. The prevailing regime depends on the production rate of vapour species
14 relative to their rate of transport away from the evaporating surface, for which an accurate theory is
15 lacking. Here, we present results of Cu and Zn isotope fractionation during evaporation of ferrobaltic
16 melts in the FeO^(T)-CaO-MgO-Al₂O₃-SiO₂ (FCMAS) system in a 1 atm gas-mixing furnace at oxygen
17 fugacities (*f*O₂) from 10⁻⁸ bar to 10^{-0.68} bar (air) at temperatures between 1300 and 1500 °C. In air, the
18 fractionation factors are $^{65/63}Cu(\alpha_{vap-liq}) = 0.9972 \pm 0.0001$ and $^{66/64}Zn(\alpha_{vap-liq}) = 0.9959 \pm 0.0002$, but
19 increase under reducing conditions, at $\log fO_2 = -8$ for $^{65/63}Cu(\alpha_{vap-liq})$ (0.9979) and at -3, -5.5 and -8 for
20 Zn, at which $^{66/64}Zn(\alpha_{vap-liq}) = 0.9967, 0.9974$ and 0.9978 , respectively. This behaviour is caused by slow
21 elemental diffusion through the silicate melt relative to the rate of evaporative loss, thereby depressing
22 $^{ij}E(\alpha_{vap-liq})$. When evaporation rates far exceed those for diffusion in the melt, no isotopic fractionation
23 develops in the condensed phase. To account for the $^{65/63}Cu(\alpha_{vap-liq})$ and $^{66/64}Zn(\alpha_{vap-liq})$ values observed
24 in air, we develop a formalism for mass transfer applicable to any evaporating species over a range of
25 pressures, gas compositions and flow regimes. For natural convection at 1 bar, diffusive transport
26 through the gas is the rate-limiting step, where $D_{(i,j)k}$ is the diffusion of isotope *i* or *j* through a gas with
27 mean molar mass M_k . Under these conditions $^{ij}E(\alpha_{vap-liq})$ is proportional to $(D_{ik}/D_{jk})^{2/3}$, and not (D_{ik}/D_{jk})
28 as previously suggested. Our model predicts $^{ij}E(\alpha_{vap-liq})$ in other experiments, and in nature, to a
29 precision of ± 0.0005 assuming ideality. The fractionation factors inferred for moderately volatile
30 elements in lunar mare basalts (>0.9994) are inconsistent with a mass transport process, and instead
31 reflect near-equilibrium conditions of vapour loss from the Moon.

32

33 *Key words:* Evaporation, Vapour, Cu, Zn, Silicate melt

34 Word count: 11441 (not including references, tables, figure captions, appendices).

35 Figures: 11

36 Tables: 4

37

38 1.0. Introduction

39 The phase transition from liquid- to gas, termed evaporation, is commonplace in geological processes.
40 Because the gas phase, as quantified by the ideal gas law, is less dense than condensed phases, mass
41 transport occurs more rapidly such that it readily escapes the system, leaving the residue depleted in
42 volatile components.

43 Two end-members styles of evaporation are classified according to the ease with which the gas phase
44 escapes (Fuchs, 1959; Chapman and Cowling, 1970). In natural processes, evaporation may fall
45 anywhere between the Langmuir (kinetic) and Knudsen (equilibrium) regimes. The former occurs when
46 each parcel of evaporating gas is perfectly and instantaneously removed from the evaporating surface,
47 and evaporation rate is therefore at a maximum (Langmuir, 1916). Knudsen evaporation, by contrast,
48 takes place when the vapour pressure of the evaporating species at the surface is equal to the equilibrium
49 partial pressure, such that the system has reached an equilibrium state (Knudsen, 1909). Physically,
50 these two regimes predominate for evaporation into a vacuum where gas escapes readily (Langmuir) or
51 in a closed system where the gas phase remains in contact with the condensed phase(s) (Knudsen). The
52 geological importance lies in the potential for the evaporative regime to give rise to different chemical
53 and isotopic signatures in the condensed phase (*e.g.*, Davis et al., 1990; Hashimoto, 1990; Humayun
54 and Cassen, 2000; Day and Moynier, 2014).

55 At high temperatures, the isotopic fractionation of volatile elements in geological materials is an ideal
56 record of evaporative style. This is because, for pure Langmuir evaporation, fractionation in the
57 abundances, X , of two isotopes, i and j of element E , between liquid (*liq*) and vapour (*vap*), defined as:

$$58 \quad {}^{i/j}E(\alpha_{vap-liq}) = \frac{({}^iX_E / {}^jX_E)_{vap}}{({}^iX_E / {}^jX_E)_{liq}}, (1)$$

59 is predictable as the inverse square root of the molar masses (M) of the evaporating species; $(M_j/M_i)^{0.5}$.
60 For the naturally-occurring isotopes, this quantity lies between 0.707 (H/D) and 0.998 ($^{207}\text{Pb}/^{208}\text{Pb}$).
61 Conversely, the isotopic fractionation at equilibrium is controlled only by the ratio of the equilibrium
62 partial pressures of the two isotopes; $p_{i,eq}/p_{j,eq}$, which, at high temperatures, is very near unity.
63 Therefore, isotopic fractionation caused by Langmuir evaporation is considerably larger than for
64 Knudsen evaporation.

65 In a geo- and cosmochemical context, semi-volatile metals, such as Cu, Zn and K (Palme et al., 1988;
66 Sossi and Fegley, 2018) provide useful insight into such processes, because of their balanced
67 partitioning between vapour and condensed phases. That the isotopic fractionation of potassium
68 observed in meteorites by Humayun and Clayton (1995) was negligible within the analytical uncertainty
69 ($\pm 0.5 \text{‰}$) was used to argue against Langmuir vaporisation as the predominant regime of vapour loss
70 in the solar nebula. This result was surprising, considering that the total pressures at the solar nebular
71 mid-plane were sufficiently low ($\sim 10^{-4}$ bar; Boss, 1998) so as to have facilitated near-pure Langmuir
72 evaporation.

73 Although subsequent studies with improved mass spectrometric methods were able to identify isotopic
74 fractionation in semi-volatile elements among a variety of terrestrial- and extraterrestrial materials
75 (Poitrasson et al., 2004; Luck et al., 2005; Moynier et al., 2006; Wombacher et al., 2008; Moynier et
76 al., 2009; Wang and Jacobsen 2016; Pringle and Moynier 2017), the fractionation factors inferred for
77 these processes were still much smaller than anticipated for evaporation into a vacuum. These results
78 precipitated renewed interest in the experimental characterisation of isotopic fractionation of semi-
79 volatile elements, particularly K, Mg and Si, in silicate melts of planetary materials under vacuum
80 conditions (Richter et al., 2002; Yu et al., 2003; Richter et al., 2007; Knight et al., 2009; Mendybaev et
81 al., 2017). Through experiment, isotopic fractionation factors in multicomponent silicate systems never
82 reached that expected for the ideal Langmuir case, $(M_j/M_i)^{0.5}$ (although see Dauphas et al. 2004 for

83 simple systems), and instead were observed to be closer to unity due to modification by *i*) the kinetics
84 of vaporisation, related to the energy barrier associated with evaporation at the surface (Hashimoto,
85 1990; Richter et al. 2002) and *ii*) the total pressure and mean molar mass of the gas medium into which
86 evaporation occurred (Richter et al. 2011).

87 The smaller isotopic fractionation factors relative to the Langmuir case inferred for semi-volatile
88 elements in lunar mare basalts (Paniello et al., 2012; Wang and Jacobsen, 2016; Boyce et al., 2018) led
89 to the realisation that isotopic signatures recorded in natural rocks are sensitive to the conditions at
90 which evaporation occurred. Wang and Jacobsen (2016) concluded that K loss during the Moon-
91 forming giant impact must have taken place at high total pressures in order to dampen the isotopic
92 fractionation factor from the Langmuir value $(M_{39}/M_{41})^{0.5} = 0.9753$ expected in a vacuum, to the ~ 0.9998
93 observed. A similar fractionation factor is also observed in Zn- (Paniello et al., 2012; Kato et al., 2015)
94 and Cu isotopes (Day et al., 2019) of mare basalts, suggesting that this is a general feature of evaporation
95 during high temperature processes.

96 Indeed, diminished isotope fractionation factors between vapour and liquid are also recorded in recent
97 impact melt glasses on Earth, formed *via* both asteroidal impacts (tektites, Moynier et al., 2009;
98 Rodovska et al., 2017; Creech et al., 2019, melt sheets, Kamber and Schoenberg, 2020) and nuclear
99 detonation (trinitites, Day et al., 2017) in which $^{i/j}E(\alpha_{vap-liq}) \geq 0.998$. To place these results into context,
100 Wimpenny et al. (2019), subjected silica-rich compositions, taken to approximate the upper continental-
101 crustal source rocks of terrestrial impact melts, to temperatures between 1600 and 2200 °C in an Ar
102 atmosphere. Although the experimentally-measured fractionation factors, $0.9988 < {}^{66/64}\text{Zn}(\alpha_{vap-liq}) <$
103 0.9998 , span those observed in impact melt glasses, the influence of thermodynamic- (oxygen fugacity,
104 temperature) relative to kinetic variables (mass transport in the gas phase, diffusion in the liquid) on the
105 fractionation factor is yet to be quantitatively addressed.

106 In order to characterise the effects of the evaporative regime on isotopic fractionation of semi-volatile
107 metals from silicate melts, we present results of Cu and Zn vaporisation experiments under controlled
108 thermodynamic conditions in a vertical tube furnace at a total pressure of 1 bar and known gas
109 composition, which is independently varied to explore the effect of oxygen fugacity. We build on the
110 combined thermodynamic-theoretical framework established in Sossi et al., (2019) to develop a
111 formalism for the effect of mass transport of the gas phase on the vaporisation rate, in order to model
112 the chemical and isotopic effects of evaporation in natural processes in a predictive manner. We apply
113 our models to assess the likely regimes of evaporative loss that were extant during tektite formation and
114 on the Moon.

115 **2.0. Methods**

116

117 *2.1. Experimental*

118 Starting materials were made from a combination of high purity (>99.9 %) oxide powders of SiO₂,
119 Al₂O₃, MgO, CaCO₃, and Fe₂O₃ in proportions of the anorthite-diopside eutectic (An₄₂Di₅₈) with ~15
120 wt. % forsterite and ~15 wt. % Fe₂O₃ to resemble a primitive natural basalt with a liquidus temperature
121 ~ 1300 °C (O'Neill and Eggins, 2002; Sossi et al., 2019). The powders were mixed together three times
122 in an agate mortar under acetone, and the ensemble was then fired overnight in a 1 atm box furnace at
123 1000 °C in air to decarbonate the mixture. The oxides of Cu and Zn were then added as oxides in order
124 to achieve ~20,000 ppm in the final mixture (Cu-Zn mix) or ~1000 ppm (Metalloids mix). The powders
125 were mixed into a slurry using 100,000 molecular weight polyethylene oxide and water, and ~25 mg
126 was smeared onto noble metal wire loops (Pt, except for experiments at or below log f O₂ -5.5, for which
127 Re was used).

128 Experiments were performed in a 1 atm GERO vertical furnace with a 4.2 cm-diameter alumina tube,
129 heated by MoSi₂ elements housed at the Institut de Physique du Globe de Paris (Sossi et al., 2019). The

130 wire loops were inserted directly into the ~3 cm-long furnace hotspot at the set temperature and desired
131 fO_2 . Temperature was digitally monitored and adjusted as necessary with a Tektronix 2110 5½ Digit
132 Multimeter connected to a Type B (Pt₇₀Rh₃₀-Pt₉₄Rh₆) thermocouple bead placed <5 mm above the
133 sample, with temperature externally set by a Eurotherm ® controller found to be stable to better than ±
134 0.5 °C. Oxygen fugacity was allowed to equilibrate for ~10 minutes prior to sample introduction and
135 was controlled by CO-CO₂ gas mixing, metered by four MKS G-series mass flow controllers (2 with
136 500 sccm full scale for CO and CO₂, 1 at 50 sccm full scale for CO, and 1 at 10 sccm full scale for
137 CO₂). The mass flow controllers were calibrated using an SIRO₂ oxygen sensor at 1000 °C, giving an
138 uncertainty of ± 0.05 log units at the mixing ratios used in the experiments. Experiments in air were
139 performed under no gas flow. Run time was recorded once the temperature reading at the thermocouple
140 reached ~99% of the set-temperature (~5 minutes) to allow the thermal mass of the sample to equilibrate
141 with the furnace atmosphere. Samples were rapidly quenched by having them drop into a bath of de-
142 ionised water.

143
144

2.2. Electron Probe MicroAnalysis

145 Quenched glass spheres were mounted, together with their wires, in epoxy and sanded down so as to
146 expose the surface of the sphere along its central axis. Electron Probe MicroAnalysis (EPMA) was
147 performed on a Cameca SX-Five Electron Microprobe, housed at CAMPARIS, Université Pierre et
148 Marie Curie, Paris, France. Analyses were carried out with a defocused electron beam of 20 µm
149 accelerated at 15 kV and with a current of 20 nA. X-ray emission was counted by five Wavelength-
150 Dispersive Spectrometers (WDS). The standards used for calibration were: anorthite (Si), albite (Na,
151 Al), periclase (Mg), haematite (Fe), diopside (Ca) and sanidine (K). Phengite was run as an internal
152 standard throughout the sequence to verify the accuracy of the ZAF correction and monitor instrumental
153 drift. Approximately 20 - 40 points per sample were made, including profiles across the sphere in order
154 to detect any zoning in major element composition.

155

2.3. Laser-Ablation Inductively-Coupled Plasma Mass Spectrometry

156 The concentrations of Cu and Zn in a subset of the experimental glasses were determined by Laser-
157 Ablation Inductively-Coupled Plasma Mass Spectrometry (LA-ICP-MS) at the Institute of
158 Geochemistry and Petrology, ETH Zürich, Switzerland (Guillong et al., 2014). The polished, epoxy-
159 mounted glasses were placed in a dual-volume Laurin Technics 155 cell filled with a 0.7 L/min He
160 carrier gas. A Resonetics Resolution 193 nm ArF excimer laser with a repetition rate of 4 Hz and a total
161 fluence of 3.5 J/cm² was used to ablate spots of 29 µm diameter. The ablation sequence consisted of 20
162 s background and 40 s of counting time, in which the ablated material was carried to the Thermo
163 Element XR magnetic sector mass spectrometer running in low resolution mode. Each mass peak is
164 measured three times (100 samples per peak with a mass window of 4%) for a total of 0.011 s each.
165 The isotopic masses measured were: ⁷Li, ²³Na, ²⁹Si, ³⁹K, ⁴³Ca, ⁴⁹Ti, ⁵⁷Fe, ⁶³Cu, ⁶⁴Zn, ⁶⁵Cu, ⁶⁶Zn, resulting
166 in one sweep every 0.465 s. The ²³²Th/¹⁶O/²³²Th ratio measured during tuning indicates that oxide
167 production was ~ 0.1 %.

168 Laser spot traverses of ~ 1,200 µm in length consisting of 10 – 12 spots each were performed from the
169 centre of the glass sphere to its edge for three glass beads, 26/12/18a, b, and c. Sample ablation was
170 bracketed by standards every ~20 points, which comprised a sequence of one NIST-610 synthetic glass
171 and two silicate glass standards (BCR-2G and GSD-1G). Standardisation was accomplished by
172 normalisation of the counts per second of a given isotope in the sample glass relative to those in NIST-
173 610 in which Cu and Zn occur at 444 ± 4 ppm and 433 ± 7 ppm, respectively (Eggins and Shelley,
174 2002). Then, the counts of ²⁹Si were normalised against those obtained by EPMA (41.7 wt. % SiO₂ in
175 samples) to correct for different ablation yields of different matrices between ferrobasaltic glasses and
176 NIST-610. Relative standard deviation (RSD) was 1.3% for Cu and 2.0 % for Zn.

177

2.4. Isotope Ratio Measurement

178 The glass spheres were broken up and separated from the noble metal wire, before being crushed into a
 179 fine powder using an agate mortar. Roughly 5 – 25 mg of powder was dissolved in a mixture of
 180 concentrated HNO₃-HCl-HF acids in Teflon beakers for 24 – 48 h at ~130 °C. The chromatographic
 181 and mass spectrometric methods follow those outlined in Sossi et al. (2015). Following complete
 182 dissolution, the samples were evaporated and re-dissolved in 6M HCl and loaded onto 1 mL of AG1-
 183 X8, Cl-form, 200-400 mesh anion exchange resin in high aspect ratio (0.4 cm radius × 7 cm length)
 184 Teflon columns. Matrix elements (Mg, Ca, Ti, and most others) are eluted by passage of 5 mL of 6 M
 185 HCl, whereas Cu is collected by another 9 mL 6 M HCl. The iron fraction was eluted by 3.5 mL of 0.5
 186 M HCl, while Zn is finally eluted with 4 mL 3 M HNO₃. Total analytical blank quantities of Cu and Zn
 187 are 1 ng, and 2 ng, respectively, negligible with respect to typical sample amounts (Cu, Zn ≈ 250 to
 188 400,000 ng).

189 The isotope composition of Cu and Zn was determined on a Thermo Neptune Plus MC-ICP-MS, housed
 190 at the Institut de Physique du Globe de Paris, with nine Faraday cups on 10¹¹ Ω resistors. Individual
 191 eluates are dissolved in 2% (0.32 M) HNO₃ and introduced into the MC-ICP-MS by means of a 50
 192 µl/min micro-flow glass nebuliser, creating an aqueous aerosol that enters a quartz-glass Scott double-
 193 pass cyclonic spray chamber before being ionised by an Ar plasma. Copper and Zn solutions are diluted
 194 to 300 ppb. In order to correct for instrumental mass bias, each sample is bracketed by an international
 195 reference material (SRM 976 for Cu and JMC-Lyon for Zn), and both samples and standards were
 196 doped with an external spike element (Ni for Cu analyses, and Cu for Zn analyses) at the same
 197 concentration as the analyte element. Copper and Zn isotope compositions are analysed in low
 198 resolution mode on flat-topped peaks. Each analysis consists of 40 integrations of 4.194 s each. Isotope
 199 ratios of Cu and Zn are expressed in delta notation, where:

$$200 \quad \delta^i E = \left(\frac{({}^i X_E / {}^j X_E)_{sample}}{({}^i X_E / {}^j X_E)_{standard}} - 1 \right) \times 1000 \quad (2)$$

201 The value of $i = 66$ or 68 for Zn and 65 for Cu, whilst the value of $j = 64$ for Zn and 63 for Cu. Solutions
 202 were run 2 – 3 times each and compared to international reference materials analysed for quality control
 203 along with the samples yielding, for BHVO-2, $\delta^{65}\text{Cu} = 0.06 \pm 0.03 \text{ ‰}$, $\delta^{66}\text{Zn} = 0.26 \pm 0.05$ and for
 204 BCR-2, $\delta^{65}\text{Cu} = 0.10 \pm 0.04 \text{ ‰}$, $\delta^{66}\text{Zn} = 0.29 \pm 0.01 \text{ ‰}$, resulting in total analytical uncertainties of \pm
 205 0.04 ‰ for $\delta^{65}\text{Cu}$ and $\pm 0.06 \text{ ‰}$ for $\delta^{66}\text{Zn}$ (both 2SD).

206

Table 1. Sample run conditions, their Cu and Zn abundances and isotope compositions relative to the starting material (SM), and modelled $\log K^*$ values.

Sample name	Temperature (°C)	CO (sccm)	CO ₂ (sccm)	log fO_2	ΔFMQ	Time (mins)	Loop	Starting mix	Cu (ppm)	lnf(Cu)	$\log K^*$	$\delta^{65}Cu_{SM}$	2SD N	Zn (ppm)	lnf(Zn)	$\log K^*$	$\delta^{66}Zn_{NSM}$	2SD $\delta^{68}Zn_{NSM}$	2SD N	
P 5/04/17b	1500	-	-	-0.68	4.72	60	Pt	Cu-Zn	6580	-0.90	-2.72	2.15	0.02 2	4983	-1.39	-2.7	5.54	0.07	10.79	0.05 2
P 10/04/17a	1500	-	-	-0.68	4.72	15	Pt	Cu-Zn	11113	-0.38	-2.50	1.03	0.02 2	9137	-0.77	-2.36	2.18	0.01	4.24	0.05 2
P10/04/17a-r	1500	-	-	-0.68	4.72	15	Pt	Cu-Zn	11113	-0.38	-2.50	0.92	0.08 2	9137	-0.77	-2.36	2.17	0.06	4.29	0.14 2
P 6/04/17c	1500	-	-	-0.68	4.72	120	Pt	Cu-Zn	3219	-1.61	-2.77	4.39	0.08 2	835	-3.16	-2.65	12.83	0.01	25.23	0.05 2
P 5/04/17a	1400	-	-	-0.68	5.62	60	Pt	Cu-Zn	9694	-0.51	-2.98	1.15	0.06 2	12403	-0.48	-3.18	1.79	0.01	3.58	0.08 2
P 7/04/17b	1400	-	-	-0.68	5.62	15	Pt	Cu-Zn				0.79	0.02 2				0.87	0.02	1.72	0.02 2
P 6/04/17b	1400	-	-	-0.68	5.62	120	Pt	Cu-Zn	6939	-0.85	-3.06	2.03	0.06 2	6884	-1.05	-3.14				
P 4/04/17c	1300	-	-	-0.68	6.62	60	Pt	Cu-Zn	13978	-0.15	-3.54	0.36	0.09 2	16860	-0.16	-3.67	0.67	0.02	1.31	0.05 2
P 6/04/17a	1300	-	-	-0.68	6.62	120	Pt	Cu-Zn	11935	-0.30	-3.52	0.57	0.10 2	13962	-0.35	-3.63	0.94	0.01	1.86	0.09 2
P 7/04/17a	1300	-	-	-0.68	6.62	15	Pt	Cu-Zn	15586	-0.04	-3.51	0.11	0.05 2	18881	-0.04	-3.62	0.30	0.04	0.60	0.04 2
P 31/07/18a	1502	-	200	-2.74	2.64	15	Pt	Cu-Zn	8888	-0.60	-2.72	1.78	0.07 3	6360	-1.13	-2.82	4.17	0.01	8.18	0.09 3
P 31/07/18b	1502	-	20	-2.74	2.64	13	Pt	Cu-Zn	10140	-0.47	-2.77	1.01	0.05 3	6892	-1.05	-2.67	3.25	0.03	6.35	0.04 3
P 21/06/18a	1500	-	200	-2.74	2.66	60	Pt	Metalloids	201	-1.60	-2.99			6	-5.07	-3.17				
P 01/08/18a	1397	-	200	-3.07	3.26	30	Pt	Cu-Zn	8533	-0.64	-3.15	1.60	0.05 3	4697	-1.44	-3.44	4.47	0.04	8.78	0.04 3
P 01/08/18b	1396.6	-	20	-3.07	3.27	29	Pt	Cu-Zn	6628	-0.89	-3.06	2.51	0.04 3	2886	-1.92	-3.29	6.04	0.06	11.78	0.14 3
P 19/06/18d	1400	-	200	-3.07	3.23	60	Pt	Metalloids	545	-0.61	-3.50			100	-2.30	-3.69	7.14	0.01	13.94	0.06 3
P 02/08/18a	1345.5	-	200	-3.26	3.57	55	Pt	Cu-Zn	7427	-0.78	-3.34	1.66	0.06 3	4434	-1.49	-3.85	4.62	0.03	9.09	0.07 3
P 19/06/18a	1299	-	200	-3.44	3.87	67	Pt	Metalloids	682	-0.38	-3.86			533	-0.63	-4.51	1.86	0.09	4.06	0.08 3
P 21/06/18b	1500	16	184	-5.50	-0.10	28	Pt	Metalloids	47	-3.06	-3.06			0.6	-7.42					
P 20/06/18a	1400	5.5	194.5	-5.51	0.79	30	Pt	Metalloids	244	-1.41	-3.45			3	-5.91					
P 22/06/18d	1400	5.5	194.5	-5.51	0.79	10	Pt	Metalloids						12	-4.30	-3.86	9.81*	0.01	19.35*	0.01 3
P 19/06/18b	1299.5	1.6	200	-5.53	1.78	29	Pt	Metalloids	468	-0.76	-3.72			215	-1.40	-4.63	3.40	0.05	6.76	0.02 3
P 01/08/18c	1396.6	6	194	-5.62	0.71	30	Re	Cu-Zn				2.88	0.08 3	5	-8.39		1.39*	0.02	2.69*	0.04 2
P 31/07/18c	1501.7	20	180	-5.70	-0.31	8	Re	Cu-Zn	4279	-1.33	-2.79	3.44	0.02 3	8	-7.83		1.75*	0.01	3.62*	0.15 2
P 3/08/18a	1347	4	196	-5.80	1.02	15	Re	Cu-Zn	7940	-0.71	-3.36	1.68	0.04 3	696	-3.35	-3.85	8.60	0.05	17.01	0.02 3
P 25/07/18a	1398	9.5	190.5	-6.02	0.30	30	Re	Cu-Zn	2277	-1.96	-3.30	5.53	0.03 3	12	-7.38		0.60*	0.07	1.32*	0.03 2
P 03/08/18b	1346.5	40.5	159.5	-7.99	-1.17	30	Re	Cu-Zn	6179	-0.96	-4.11	2.18	0.02 3	122	-5.09	-5.35	11.10	0.03	21.86	0.05 3
P 31/07/18d	1500.5	121.5	78.5	-8.00	-2.60	12	Re	Cu-Zn	303	-3.98	-3.15	8.81	0.07 3	7	-7.98		1.91*	0.11	4.00*	0.18 2
P 19/06/18c	1299	24	176	-8.00	-0.69	17	Re	Metalloids	325	-1.12	-3.93			26	-3.51	-5.11	7.44	0.06	14.54	0.08 2
P 21/06/18c	1500	121.5	78.5	-8.00	-2.60	14	Re	Metalloids	12	-4.42	-3.23			0.5	-7.60					
P 22/06/18b	1500	121.5	78.5	-8.00	-2.60	7	Re	Metalloids						7	-4.81		8.70*	0.08	16.53*	0.10 2
P 20/06/18b	1398	67	133	-8.03	-1.71	13	Re	Metalloids	91	-2.39	-3.48			0.4	-7.82					
P 01/08/18d	1396.6	66.5	133.5	-8.04	-1.70	30	Re	Cu-Zn	62	-5.56	-3.50	11.96	0.09 3	11	-7.45		1.11*	0.01	2.15*	0.04 2
<i>Stand-alone experiments</i>																				
P 26/12/18a	1300	2.7	197.3	-5.99	1.31	10	Re	Cu-Zn	9137	-0.57				9421	-0.54					
P 26/12/18b	1300	2.7	197.3	-5.99	1.31	20	Re	Cu-Zn	4786	-1.22				2860	-1.73					
P 26/12/18c	1300	24	176	-8.00	-0.69	5	Re	Cu-Zn	5321	-1.11				2256	-1.97					

*denotes samples affected by contamination; N = number of replicates; ΔFMQ = log unit deviation in fO_2 from the Fayalite-Magnetite-Quartz buffer; sccm = standard cubic centimetres per minute

209

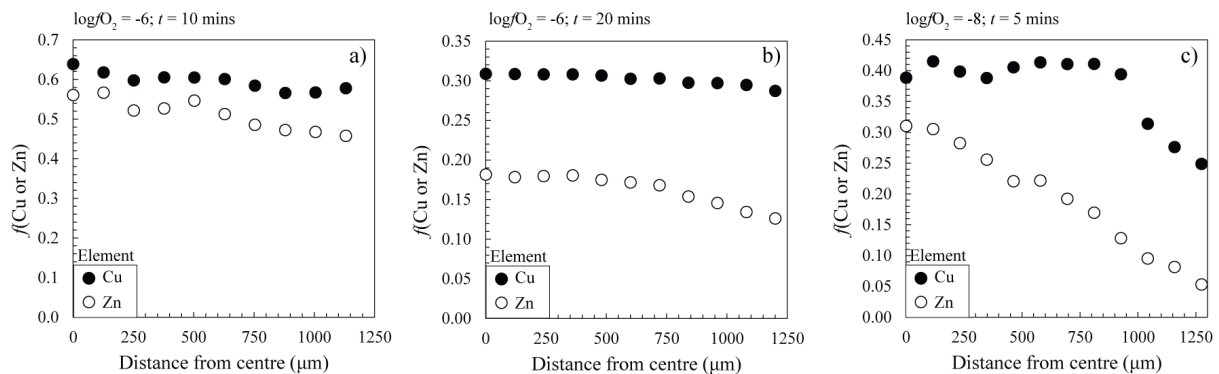
210 **3.0. Results**

211

212 **3.1. Experimental Glasses**

213 A subset of glasses run at 1300, 1400 and 1500 °C, each at three $\log fO_2$ (-3, -5.5 and -8), totalling nine
 214 samples, were analysed for their major element composition by EPMA. Samples at 1400 °C and 1500
 215 °C quenched to glass spheres of $\approx 1000 \mu\text{m}$ radius; whereas those performed at 1300 °C contained ~ 5
 216 wt. % of olivine \pm spinel crystals, as calculated by mass balance. The major element compositions of
 217 the wholly glassy experiments ($T > 1300$ °C) are homogeneous, with an average (expressed as wt. %
 218 oxide) of $41.70 \pm 0.30 \text{ SiO}_2$, $10.60 \pm 0.07 \text{ Al}_2\text{O}_3$, $15.54 \pm 0.11 \text{ MgO}$, $14.58 \pm 0.30 \text{ FeO}^T$, and $17.59 \pm$
 219 0.41 CaO . The composition of each glass is reported in *Supplementary Table S1*.

220 No zoning in major elements as a function of sphere radius is observed due to their being non-volatile
 221 at the experimental conditions. Three standalone experiments were run at 1300 °C for 10 and 20 minutes
 222 at $\log fO_2 = -6$, and for 5 minutes at $\log fO_2 = -8$, in order to assess the degree of zoning of Cu and Zn at
 223 low temperatures and low fO_2 , where zoning should be most prevalent because the diffusion rate of the
 224 volatile species through the melt decreases with temperature, while evaporation rate increases at more
 225 reducing conditions (Sossi et al., 2019). Copper contents vary by $<10\%$ between the edge and the centre
 226 of experiments run at $\log fO_2 = -6$ (Fig. 1a, b), whereas at $\log fO_2 = -8$ the outer $300 \mu\text{m}$ display a decrease
 227 in concentration by up to 40 % relative to the interior (Fig. 1c). Zinc concentrations are zoned in all
 228 three experiments; with $Zn_{\text{rim}}/Zn_{\text{core}}$ of 0.8 to 0.7 at $\log fO_2 = -6$ (Fig. 1a, b), and more markedly at $\log fO_2$
 229 -8 , where they are six times lower in the rim than in the core (Fig. 1c). Data for each zoning profile is
 230 presented in *Supplementary Table S2*.



231

232 **Figure 1.** The fraction of Cu or Zn remaining in the glass as a function of distance from the centre of the sphere
 233 (in μm) after evaporation at 1300 °C at **a)** $\log fO_2 = -6$, $t = 10$ minutes, **b)** $\log fO_2 = -6$, $t = 20$ minutes, and **c)**
 234 $\log fO_2 = -8$, $t = 5$ minutes. Cu = black circles, Zn = white circles.

235 **3.2. Copper and Zinc concentrations**

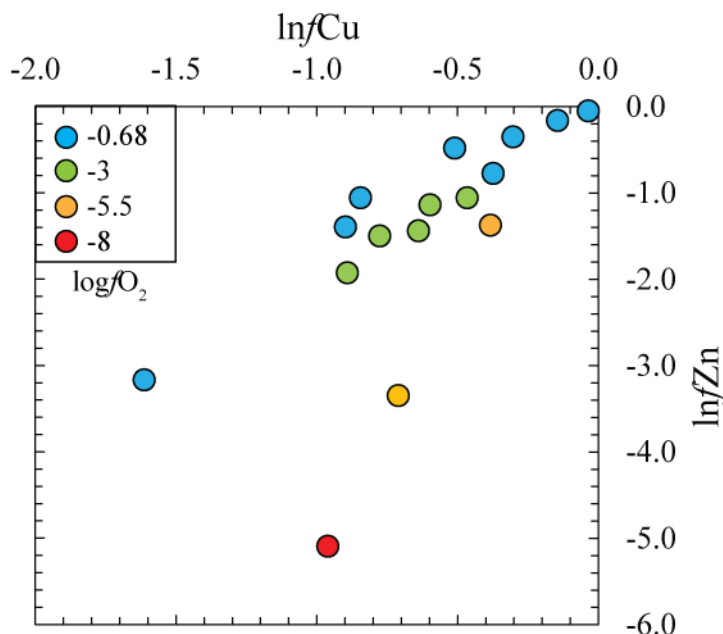
236 In the two starting mixtures, labelled ‘Metalloids’ and ‘Cu-Zn’, Cu is present at 944 ± 12 ppm and
 237 16177 ± 188 ppm, respectively, whereas Zn concentrations are 974 ± 21 ppm and 19747 ± 178 ppm.
 238 Bulk copper contents in the experimental glasses of the ‘Metalloids’ mix are between 682 ppm (run
 239 P19/06/18a) and 12 ppm (run P21/06/18c), while those for the ‘Cu-Zn mix’ fall within the range of
 240 15586 ppm (run P07/04/17a) to 62.3 ppm in run P01/08/18d. Bulk zinc contents of the experimental
 241 glasses range from 533 ppm (run P19/06/18a) to 0.5 ppm (run P21/06/18c) in the ‘Metalloids’ mix and
 242 from 18881 ppm (run P07/04/17a) to 4.5 ppm in run P01/08/18c for the ‘Cu-Zn’ mix (Table 1).

243 Element depletions in the glasses are expressed as $f(E)$ ($E = \text{Cu or Zn}$), where:

$$244 \quad f(E) = \frac{X_E^t}{X_E^0} \quad (3)$$

245 Where X_E refers to the concentration of the element E in the glass at time t and at time 0, respectively.

246 Calculated values of $\ln f_{\text{Cu}}$ and $\ln f_{\text{Zn}}$ positively co-vary and form discrete linear trends at $\log f_{\text{O}_2}$ -0.68
 247 and -3 with intercepts within uncertainty of 0 (Fig. 2). For experiments in air, the relative depletion of
 248 Zn relative to Cu ($\ln f_{\text{Zn}}/\ln f_{\text{Cu}}$) is approximately unity, meaning that both Zn and Cu vaporise to similar
 249 extents. The average value is 1.12 ± 0.12 ($N = 5$) for experiments in air at 1300 °C and 1400 °C, while
 250 relatively more Zn depletion is observed for the series at 1500 °C (1.85 ± 0.27 , $N = 3$). This behaviour
 251 is predicted thermodynamically for the evaporation of Cu and Zn from basaltic melts, for which the
 252 vapour pressure of Zn increases more rapidly with temperature than does that of Cu (Sossi et al., 2019).
 253



254
 255 **Figure 2.** A plot of the natural logarithm of the fraction of Cu remaining in the melt ($\ln f_{\text{Cu}}$) compared with that
 256 of Zn ($\ln f_{\text{Zn}}$) in a given experiment for the Cu-Zn mix. The points form roughly linear arrays in log-log space for
 257 a given f_{O_2} , colour-coded by blue = air, green = pure CO_2 ($\log f_{\text{O}_2} \sim -3$), yellow = $\log f_{\text{O}_2} -5.5$, red = $\log f_{\text{O}_2} -8$.
 258 The points qualitatively show that Zn becomes relatively more volatile with respect to Cu at lower f_{O_2} s, as
 259 expected according to their reaction stoichiometries. The effect of temperature is to favour Zn loss relative to Cu,
 260 though this is minor between 1300 °C and 1500 °C compared to changing f_{O_2} . Longer run times and higher
 261 temperatures result in a decrease in both $\ln f_{\text{Cu}}$ and $\ln f_{\text{Zn}}$ at a given $\log f_{\text{O}_2}$.

262 Experiments performed at lower oxygen fugacities are sparse and do not permit assessment of any
 263 temperature dependence. However, with decreasing f_{O_2} , $\ln f_{\text{Zn}}/\ln f_{\text{Cu}}$ increases from 2.09 ± 0.17 ($N =$
 264 5) in pure CO_2 experiments ($\log f_{\text{O}_2} \approx -3$), 4.53 ± 0.86 ($N = 3$) at $\log f_{\text{O}_2} \approx -5.5$ and the single reliable
 265 point at $\log f_{\text{O}_2} -8$ gives 5.30 (Fig. 2). The dependence of $\ln f_{\text{Zn}}/\ln f_{\text{Cu}}$ with f_{O_2} stems from the
 266 stoichiometry of their respective vaporisation reactions. Copper is present as $\text{CuO}_{0.5}$ in silicate melts
 267 (i.e., monovalent) and Zn occurs in divalent form as ZnO. However, the stable gas species of both is
 268 the monatomic gas (that is, Cu^0 and Zn^0 ; Lamoreaux et al., 1987) and their vaporisation reactions from
 269 silicate melts are therefore written:



271 and, for Zn:

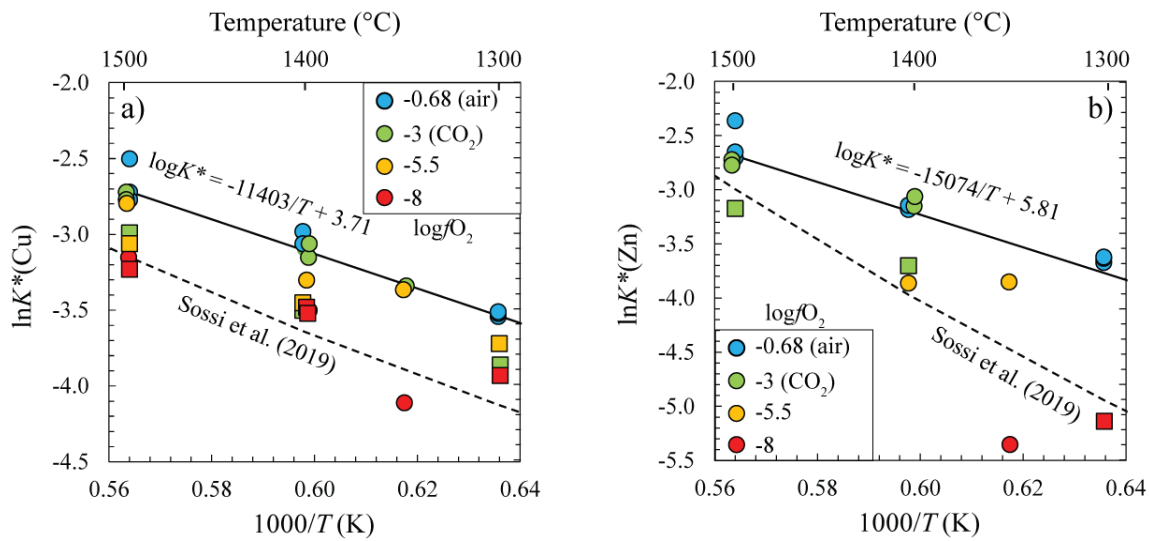


273 The $n = 1$ reaction of Cu means that the vapour pressure of Cu(g), p_{Cu} , is proportional to $(f\text{O}_2)^{-1/4}$
 274 whereas p_{Zn} depends on $(f\text{O}_2)^{-1/2}$. Therefore, lower oxygen fugacities will promote relatively more Zn
 275 vaporisation with respect to Cu, resulting in progressively higher $\ln f_{\text{Zn}}/\ln f_{\text{Cu}}$, proportional to $(f\text{O}_2)^{-1/4}$.

276 In detail, the degree of elemental loss of both Cu and Zn depends on the physical properties of the
 277 silicate melt sphere, the experimental run time and the effective equilibrium constant of the reaction
 278 (K^*). To quantify the effects of these variables on elemental loss, we perform a non-linear least-squares
 279 minimisation to $\ln f(E)$ measured experimentally by varying K^* ($=K\gamma_{\text{ev}}\gamma_i$, where K is the equilibrium
 280 constant for reactions (4) and (5) in their standard states at T and 1 bar, γ_{ev} is the evaporation coefficient
 281 and γ_i is the activity coefficient of the melt oxide component) in the equation developed by Sossi et al.
 282 (2019):

$$283 \quad \ln f(E) = \left(-\frac{K^*}{f(\text{O}_2)^{n/4}} \frac{3M}{r\rho} \sqrt{\frac{1}{2\pi M_i RT}} (t - t_0) \right). \quad (6)$$

284 Where n refers to the number of electrons exchanged in the vaporisation reaction (set equal to 1 for Cu
 285 and 2 for Zn; eqs. (4) and (5)). Other factors in the equation are known or controlled in each experiment;
 286 r the radius of the sphere, ρ its density, M and M_i are the molar mass of the sphere and of the evaporating
 287 species respectively, R the gas constant, T the absolute temperature, t the experimental run time and t_0
 288 the time at which the element begins evaporating. This treatment invokes equilibrium only insofar as
 289 equations (4) and (5) are presumed to accurately describe the evaporation reactions occurring at the
 290 melt surface (as verified experimentally; Sossi et al., 2019), and the $f\text{O}_2$ of the melt is that imposed by
 291 the gas mixture. However, activity and evaporation coefficients of the evaporating species, as quantified
 292 by fits to the experimental data with the K^* term, may deviate from unity, and hence from the
 293 equilibrium conditions of Knudsen evaporation (e.g., Hoenig and Searcy, 1966).



294
 295 **Figure 3.** Fitted values of $\log K^*$ expressed as a function of inverse temperature ($1000/T$) in Kelvin for **a)** Cu and
 296 **b)** Zn. Each point corresponds to a single experiment, where $\log K^*$ is calculated by minimising the misfit to the
 297 measured $\ln f(E)$ using equation (6). The colour corresponds to a different oxygen fugacity, as in Fig. 2, while
 298 circles stand for the ‘Cu-Zn’ mixture and squares the ‘Metalloids’ mixture. The straight line fits are calculated
 299 from linear regressions to the data (T in K) for the ‘Cu-Zn mix’ (this work, solid line), excluding points at $\log f\text{O}_2$
 300 $= -8$ and -5.5 (for Zn) and $\log f\text{O}_2 = -8$ (for Cu), and to the data of Sossi et al. (2019) (dashed line).

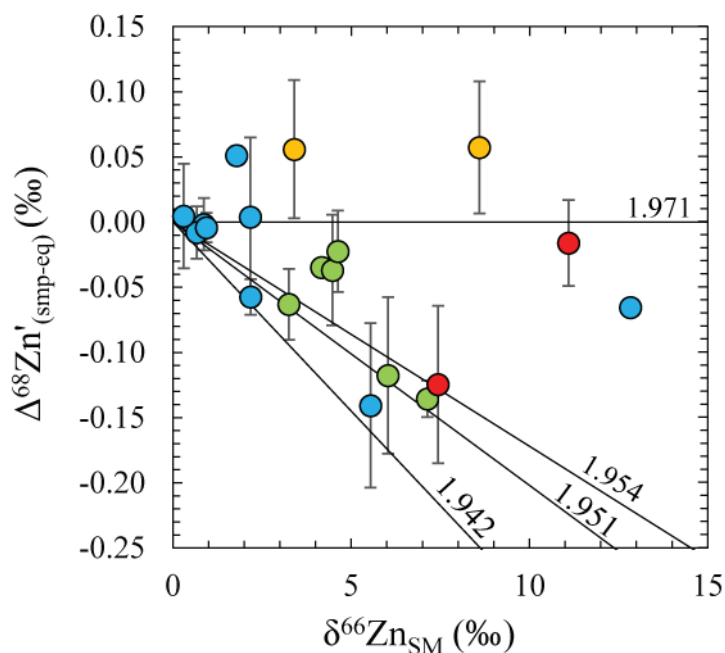
301 The $\log K^*$ of reaction for both Cu and Zn define a linear relationships with inverse temperature,
 302 expressed as $1000/T$ (Fig. 3), ranging from ~ -3.5 at 1300°C to ~ -2.5 at 1500°C , where an increase
 303 denotes that the vapour species is increasingly favoured (eqs. 4, 5). Compared with the $\log K^*$ values in
 304 Sossi et al. (2019), in which silicate melts containing 1000 ppm Cu and Zn were evaporated, the $\log K^*$
 305 calculated herein is generally ~ 0.5 log units higher. This is also verified from measurements of the

306 ‘Metalloids’ mixture (~1000 ppm) which plot near the Sossi et al. (2019) determination, suggesting this
 307 difference is likely because CuO_{0.5} and ZnO in the Cu-Zn melts (~20,000 ppm) are no longer in the
 308 Henry’s Law region, resulting in differences in their activity coefficients. Also evident is a systematic
 309 decrease in log*K** as a function of log*f*O₂ for both Cu (at log*f*O₂ -8) and Zn (at or below log*f*O₂ -5.5).
 310 This attests to a decrease in the evaporation rate at that oxygen fugacity compared to that anticipated
 311 from equation (6) with *n* = 1 for Cu and *n* = 2 for Zn, for which log*K* should be independent of the *f*O₂.

312 3.3. Copper and Zinc isotope ratios

313 The starting material (SM) has δ⁶⁵Cu of +0.09 ± 0.02 ‰ (CuO, Alfa Aesar) relative to SRM-976 and
 314 δ⁶⁶Zn = +0.16 ± 0.02 ‰ (ZnO, Alfa Aesar) relative to JMC-Lyon. All isotopic ratios are reported
 315 relative to those of the starting materials (δ^xE_{SM}), and are summarised in Table 1. Values of δ⁶⁵Cu_{SM}
 316 range from +0.11 ± 0.05 ‰ (run P07/04/17a) to +11.96 ± 0.09 ‰ (run P01/08/18d) and for δ⁶⁶Zn_{SM}
 317 vary between +0.30 ± 0.04 ‰ (run P07/04/17a) to +12.83 ± 0.01 ‰ (run 06/04/17c).

318 All experiments had sufficient quantities of Cu remaining in the glass to permit their isotopic analysis.
 319 For Zn, however, higher temperature experiments (≥1400 °C) at reducing conditions (log*f*O₂ -5.5 and -
 320 8) and longer run times (> 10 minutes) were poor in Zn. These samples, marked with an asterisk in
 321 Table 1, deviate considerably from the ln*f*(E) vs. δ^xE trends defined by the other samples, indicative of
 322 contamination by exchange with the furnace atmosphere (see *Supplementary Information*) and are not
 323 discussed further. The slope in δ⁶⁸Zn vs. δ⁶⁶Zn space is 1.962±0.008 with an intercept of -0.032 ± 0.041
 324 (N = 20). The value of the slope theoretically reflects the mass fractionation law governing isotope
 325 fractionation, with an equilibrium process giving rise to a slope of 1.971 in δ⁶⁸Zn vs. δ⁶⁶Zn space
 326 whereas purely kinetic fractionation yields 1.942. Following the approach of Young and Galy (2004)
 327 and Wombacher et al. (2011), this dependence is better resolved in a plot of Δ⁶⁸Zn’_(smp-eq) vs. δ⁶⁶Zn (Fig.
 328 4), where Δ⁶⁸Zn’_(smp-eq) = δ⁶⁸Zn_{smp} - δ⁶⁶Zn_{smp} × 1.971, and ‘smp’ denotes the measured value. Although
 329 some samples appear to follow the kinetic trend defined for the masses or reduced masses of Zn in air
 330 (1.951) or CO₂ (1.954), deviation from the equilibrium line shows no apparent dependence on the log*f*O₂
 331 or temperature at which the sample equilibrated.



332
 333 **Figure 4.** The Δ⁶⁸Zn’_(smp-eq) vs. δ⁶⁶Zn_{SM} of the experimental glasses. The slope of the line in δ⁶⁸Zn_{SM} vs. δ⁶⁶Zn_{SM}
 334 space is sensitive to the mode of isotopic fraction, in which, for the harmonic approximation, the kinetic and
 335 equilibrium end-members define slopes of 1.971 (a horizontal line in this representation) and 1.942, respectively.
 336 For kinetic transport in a diffusion-limited regime, the slope depends on the reduced masses, which gives 1.951

337 for ambient gas with the molar mass of air (0.029 kg/mol), and 1.954 in pure CO₂ (0.044 kg/mol). Colours denote
 338 the fO_2 of the experiment and are as per Fig. 1. Error bars are shown as 2SD.

339

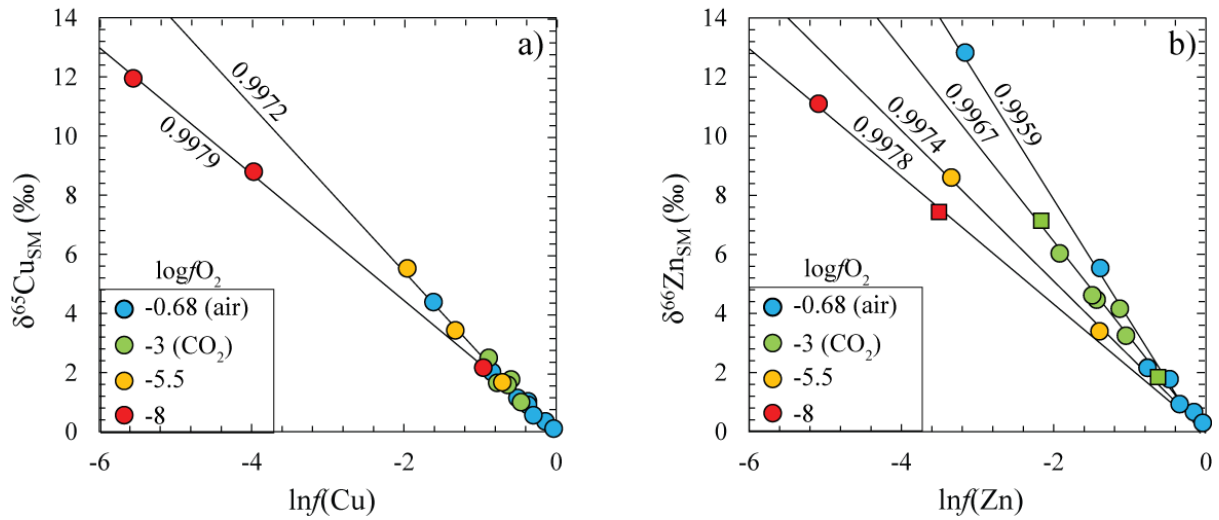
340 For the isotopic evolution of a homogeneous and finite reservoir, the Rayleigh equation cast in terms
 341 of isotopic fractionation is written:

$$342 \frac{{}^iX_{E,liq}^t / {}^jX_{E,liq}^t}{{}^iX_{E,liq}^0 / {}^jX_{E,liq}^0} = \frac{{}^{i/j}R_{E,liq}^t}{{}^{i/j}R_{E,liq}^0} = f_E ({}^{i/j}E_{\alpha_{vap-liq}})^{-1}. \quad (7)$$

343 The fractionation factor may be calculated from measured data according to the approximation:

$$344 {}^{i/j}E(\alpha_{vap-liq}) = \left(\left(\frac{\delta^{i/j}E_{liq}}{\ln f_E} \right) \frac{1}{10^3} \right) + 1. \quad (8)$$

345 Thus, the isotopic fractionation factor is determined by plotting $\delta^{65}\text{Cu}$, $\delta^{66}\text{Zn}$ or $\delta^{68}\text{Zn}$ against $\ln f(\text{Cu}$ or
 346 $\text{Zn})$ (Fig. 5a, b).



347

348 **Figure 5.** The isotopic composition of **a)** Cu, expressed as $\delta^{65}\text{Cu}_{\text{SM}}$ and **b)** Zn, expressed as $\delta^{66}\text{Zn}_{\text{SM}}$ (where ‘SM’
 349 denotes the per mille deviation from the starting material), as a function of their respective relative abundances
 350 remaining in the glass, $\ln f(\text{Cu})$ and $\ln f(\text{Zn})$. Circles correspond to the ‘Cu-Zn’ mix, and squares to the ‘metalloids’
 351 mix. The thin black lines are regressions through the data; for Cu, all data fall on a single line with a fractionation
 352 factor, ${}^{65/63}\text{Cu}(\alpha_{vap-liq}) = 0.9972$, save for the three samples equilibrated at $\log fO_2 = -8$, which define ${}^{65/63}\text{Cu}(\alpha_{vap-}$
 353 $liq) = 0.9979$. For Zn, ${}^{66/64}\text{Zn}(\alpha_{vap-liq})$ decreases as a function of fO_2 , from 0.9959 in air, 0.9967 at $\log fO_2 \approx -3$,
 354 0.9974 at $\log fO_2 \approx -5.5$ and 0.9978 at $\log fO_2 = -8$.

355 For Cu, there is no correlation between ${}^{65/63}\text{Cu}(\alpha_{vap-liq})$ and temperature or run duration. For ${}^{65/63}\text{Cu}(\alpha_{vap-}$
 356 $liq)$ calculated for different fO_2 series (-0.68, -3, -5.5, -8), the three most oxidised series define the same
 357 fractionation factor, 0.9972 ± 0.0001 (N = 17) (Fig. 5a), whereas at $\log fO_2 = -8$ the fractionation factor is
 358 smaller, ${}^{65/63}\text{Cu}(\alpha_{vap-liq}) = 0.9979 \pm 0.0001$ (N = 3). Both series have intercepts ($\delta^{65}\text{Cu}_0$) very near 0; -
 359 0.18 ± 0.08 ‰ and $+0.17 \pm 0.21$ ‰, respectively. For Zn, both Cu-Zn and Metalloids mixes give
 360 consistent values, with a difference in ${}^{66/64}\text{Zn}(\alpha_{vap-liq})$ observed at each $\log fO_2$; 0.9959 ± 0.0002 (N = 8)
 361 at -0.68, 0.9967 ± 0.0002 (N = 7) at -3, 0.9974 (N = 2) at -5.5 and 0.9978 (N = 2) at -8 (Fig. 5b). At
 362 $\log fO_2 = -0.68$, $\delta^{66}\text{Zn}_0$ is -0.35 ± 0.23 ‰ while $\delta^{66}\text{Zn}_0 = -0.07 \pm 0.34$ ‰ at $\log fO_2 = -3$, whereas the two
 363 reducing series had their intercept forced through 0 due to the lack of points. Regressions not forced
 364 through the origin yield ${}^{66/64}\text{Zn}(\alpha_{vap-liq}) = 0.9973$ and 0.9977 at $\log fO_2 = -5.5$ and -8, respectively.

365 4.0. Discussion

366
367
368

4.1. Diffusion and the effect of oxygen fugacity on elemental loss and the vapour-liquid fractionation factor

369 The observation that the apparent isotopic fractionation factors of Cu and Zn between liquid silicate
370 and the gas phase decrease as a function of oxygen fugacity behoves an explanation. Over the range of
371 fO_2 investigated, thermodynamic stability of the gas species for Cu and Zn should remain unchanged,
372 with Cu^0 and Zn^0 predominating under all conditions (Lamoreaux et al., 1987; Sossi et al., 2019).
373 Although Cu may also exist in its 2+ oxidation state in silicate melts at high oxygen fugacities (*e.g.*, in
374 air), the observed shift in $^{65/63}Cu(\alpha_{vap-liq})$ occurs at $\log fO_2$ between -6 and -8; too reducing for Cu^{2+} to be
375 stable (Holzheid and Lodders, 2001). On the other hand, Zn only exists as Zn^{2+} at all oxygen fugacities,
376 meaning the systematic change in fractionation factor is not readily ascribed to a change in liquid or gas
377 speciation as a function of fO_2 .

378 The shift does coincide, however, with the appearance of zonation in both elements in the melts; for the
379 experiment at $\log fO_2$ -8 and 1300 °C (26/12/18c) for Cu, and below $\log fO_2$ -6 for Zn (26/12/18a, b; Fig.
380 1). Formation of such a chemical and isotopic boundary layer at the evaporating surface may cause
381 deviations of the fractionation factor between vapour – liquid inferred from the measurement of the
382 bulk glass relative to cases in which the glass is homogeneous. The magnitude and sense of this isotopic
383 divergence depend on the relative timescale of the element's evaporation rate *vs.* its homogenisation
384 rate in the melt (which, for a sphere in the absence of a thermal gradient, can only occur by diffusion)
385 and the difference in diffusion rates between the two isotopes in the melt (Young, 2000; Richter, 2004;
386 Moynier et al., 2009).

387 Thus, if the vaporisation rate at the surface is known, the elemental zoning profiles, in conjunction with
388 the observed $^{65/63}E(\alpha_{vap-liq})$, can be used to derive *i*) the elemental diffusion coefficient, D and *ii*) the relative
389 differences in diffusion coefficients between two isotopes through the silicate melt. In order to do so, a
390 central finite difference discretisation diffusion model in spherical co-ordinates (Crank, 1975; Ford-
391 Versypt and Braatz, 2014) is implemented (*Appendix A1*). The model approximates the diffusion of an
392 element or isotope through the silicate melt medium with a time-dependent boundary condition set by
393 its evaporation at the surface of the bead.

394 The K^* value in eq. 6 is varied in order to produce the correct value of $X_{Cu,Zn}^t$ observed at the surface,
395 taken to represent the steady-state value due to evaporation. Then, the value of D is varied in order to
396 minimise the misfit to the objective function;

397
$$\chi^2 = \frac{\Sigma(X_{Cu,Zn,r}^t(obs) - X_{Cu,Zn,r}^t(calc))^2}{\Sigma\sigma(obs)} \quad (9)$$

398 Where χ^2 quantifies the sum of the misfit between the normalised concentration at each value of r
399 (radial distance from the centre of the bead) that are observed (obs) and calculated by the model (calc)
400 given the experimental run time, t . Results are shown in Table 2 and Fig. 6.

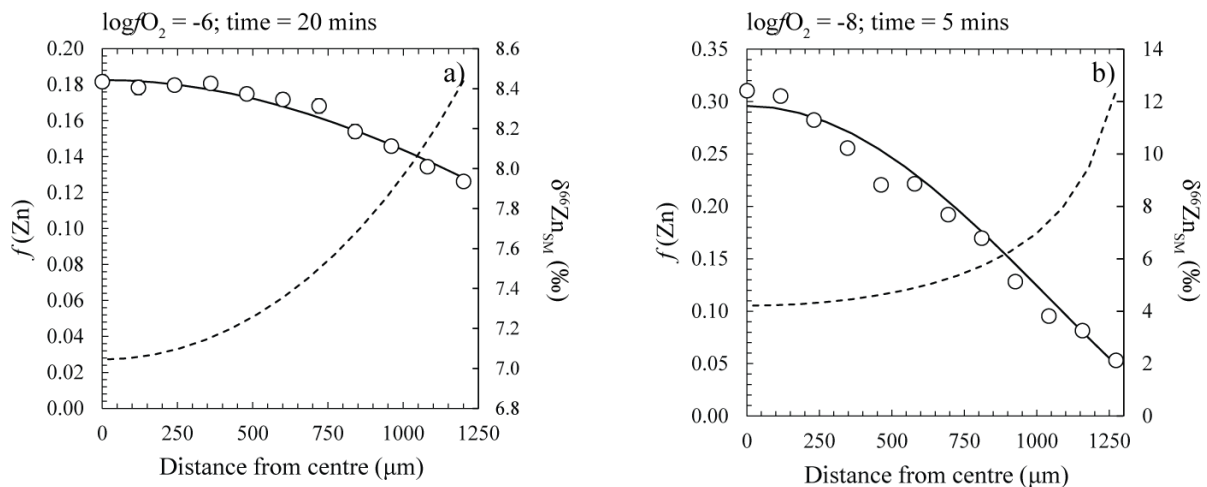
401 The fitted diffusion coefficient of Zn in ferrobasic melt is consistent among the three experiments,
402 $1.56 \pm 0.25 \times 10^{-9} \text{ m}^2/\text{s}$ at 1300 °C. There are no measurements of Zn diffusion coefficients in relevant
403 compositions, however, tracer diffusivities of other divalent metal cations (Co^{2+} , Mn^{2+}) in basaltic melts
404 are $\sim 10^{-10} \text{ m}^2/\text{s}$ (Lowry et al., 1982) at the same temperature. For Cu, the value of $2.61 \times 10^{-9} \text{ m}^2/\text{s}$
405 determined herein from a single experiment is nearly an order of magnitude higher than measured by
406 Ni and Zhang (2016) in a basaltic melt at 1300 °C ($\sim 4 \times 10^{-10} \text{ m}^2/\text{s}$). However, given the empirical
407 dependence of $\log D$ on $1/\eta$ (*e.g.*, Mungall, 2002), and the factor of 10 lower viscosity of the melt
408 composition used here, $\sim 2.3 \text{ Pa.s}$, compared to the experimental basaltic melts of Lowry et al. (1982)
409 and Ni and Zhang (2016), both $\sim 27 \text{ Pa.s}$ at 1300 °C, the values of D would be expected to be an order
410 of magnitude higher.

411 Isotopic composition is predicted by constructing two finite difference profiles; one for each isotope.
 412 The fractionation factor between liquid and vapour at the boundary of sphere is modified by adjusting
 413 the ratio of the equilibrium constants of the isotope vaporisation reactions (K^*/K^* ; eqs. A4 and A5) to
 414 yield the expected value of $^{ij}E(\alpha_{vap-liq})_{surf}$ under conditions that are not diffusion-limited (*i.e.*, in air;
 415 0.9959 for $^{66/64}Zn$, 0.9972 for $^{65/63}Cu$). Tracer diffusivity of two isotopes in a given medium is
 416 proportional to the inverse ratio of their masses, related by an exponent, β , *i.e.*, $(M_j/M_i)^\beta$. Because the
 417 isotopic composition of the bulk sample is unknown, β cannot be determined independently, and must
 418 be assumed. By analogy with the diffusion of other divalent first-row transition metal cations in silicate
 419 melts, we adopt a value of $\beta = 0.015 \pm 0.010$ (Richter et al., 2009). This results in an isotopic
 420 fractionation factor due to diffusion, $^{ij}E(\alpha_{diff})$ of 0.9998 ($\beta = 0.005$) to 0.9993 ($\beta = 0.025$).

Table 2. A summary of the experimental conditions of the 26/12/18a-c set of experiments ($T = 1300$ °C) measured for elemental zoning profiles, and the associated model parameters and results, assuming $\beta = 0.015$.

	26/12/18a	26/12/18b	26/12/18c	
$\log fO_2$	-6	-6	-8	
Time (mins)	10	20	5	
Element	Zn	Zn	Zn	Cu
D_0 (m^2/s)	$1.56(0.18) \times 10^{-9}$	$1.25(0.08) \times 10^{-9}$	$1.75(0.05) \times 10^{-9}$	$2.61(0.33) \times 10^{-9}$
$f(Zn \text{ or } Cu)_{surf}$	0.46	0.13	0.05	0.25
$f(Zn \text{ or } Cu)_{bulk}$	0.49	0.15	0.12	0.31
$\log K^*_{surf}$	-4.84	-4.73	-4.96	-3.30
$\log K^*_{bulk}$	-4.88	-4.76	-5.11	-3.37
t_{evap} (s)	1176	1379	316	435
$\delta^{66}Zn / \delta^{65}Cu$ (‰) (calc)	2.93	7.88	6.85	3.16
$^{ij}E(\alpha_{vap-liq})_{surf}$ (assumed)	0.9959	0.9959	0.9959	0.9972
$^{ij}E(\alpha_{vap-liq})_{bulk}$ (calc)	0.9959	0.9959	0.9968	0.9973

421



422

423 **Figure 6.** Laser-Ablation ICP-MS data for Zn abundances (white circles) as a function of core (0 μm) to rim
 424 (~ 1200 μm) in experimental glass spheres synthesised at 1300 °C; **a)** 26/12/18b, $t = 20$ mins, $\log fO_2 = -6$ and **b)**
 425 26/12/18c, $t = 5$ mins, $\log fO_2 = -8$. Overlain on the data are, on the primary ordinate axis, the finite-difference
 426 model fit to the Zn abundances measured (solid black curve), and on the secondary ordinate axis, the modelled
 427 $\delta^{66}Zn_{SM}$ evolution with $\beta = 0.015$ as a function of radius (dashed black curve). The boundary condition is set by
 428 evaporative loss according to eq. (6) for both ^{66}Zn and ^{64}Zn , with the constraint that vaporisation rates at the
 429 surface are $^{66/64}Zn(\alpha_{vap-liq}) = 0.9959$.

430 For $\beta = 0.015$, the isotopic composition of Zn (or Cu) in the centre of the bead is lighter than at the
 431 boundary, where $^{ij}E(\alpha_{vap-liq})_{surf}$ is fixed (Fig. 6). This may seem counterintuitive, because the lighter
 432 isotope is able to diffuse more quickly than the heavier isotope, and therefore reaches the surface more
 433 rapidly. However, the key factor controlling whether the interior of the bead is isotopically heavy or
 434 light relative to the surface is the ratio of isotopic fractionation factor due to diffusion, $^{ij}E(\alpha_{diff})$ to the

435 isotopic fractionation factor due to evaporation, $^{i/j}E(\alpha_{vap-liq})$. Where $^{i/j}E(\alpha_{diff}) > ^{i/j}E(\alpha_{vap-liq})_{surf}$, evaporation
 436 induces larger isotopic fractionation than can be compensated for by the faster diffusion of the lighter
 437 isotope relative to the heavier isotope, and the interior remains lighter than the rim, yet both are enriched
 438 relative to the initial composition. This causes the bulk $^{i/j}E(\alpha_{vap-liq})_{bulk}$ value to increase (i.e., smaller
 439 fractionation) relative to that predicted by $^{i/j}E(\alpha_{vap-liq})_{surf}$ (Table 2). However, as β increases such that
 440 $^{i/j}E(\alpha_{diff}) < ^{i/j}E(\alpha_{vap-liq})_{surf}$, then $^{i/j}E(\alpha_{vap-liq})_{bulk}$ is lower (i.e., larger fractionation factor) than $^{i/j}E(\alpha_{vap-liq})_{surf}$,
 441 because the heavier isotope is unable to diffuse sufficiently rapidly to the surface, and becomes
 442 increasingly concentrated in interior of the bead. This phenomenon is illustrated graphically in Fig. A1.

443 At the constant value of $\beta = 0.015$ used to model the data, then, the degree to which $^{i/j}E(\alpha_{vap-liq})_{bulk}$
 444 increases (i.e., fractionation factor becomes closer to unity) relative to $^{i/j}E(\alpha_{vap-liq})_{surf}$ is proportional to
 445 the timescale of evaporation relative to diffusion, denoted t_{diff}/t_{evap} . Experimental charges at $\log fO_2$ -6
 446 are predicted to show only little- to modest changes in $^{i/j}E(\alpha_{vap-liq})_{bulk}$ compared to $^{i/j}E(\alpha_{vap-liq})_{surf}$, as
 447 illustrated by the similar isotope composition of their interiors relative to the boundary layer (Fig. 6a).
 448 On the other hand, $\delta^{66}Zn$ is predicted to be lower by $\sim 8\%$ in the interior relative to the rim in the run
 449 at $\log fO_2$ -8 (Fig. 6b), causing an increase in $^{i/j}E(\alpha_{vap-liq})_{bulk}$ (0.9968) relative to $^{i/j}E(\alpha_{vap-liq})_{surf}$ (0.9959).
 450 Given that the diffusion rate is near-constant with fO_2 (Table 2) and temperature is constant, this
 451 phenomenon arises due to the faster evaporation rate of Zn at low fO_2 (eq. 5). The characteristic
 452 evaporation timescale, t_{evap} (i.e., the time taken to evaporate $(1-f(E)_{surf})$ relative to the experimental run
 453 time, t_{exp}), is given by:

$$454 \quad t_{evap} = \frac{t_{exp}}{(1-f(E)_{surf})} (10)$$

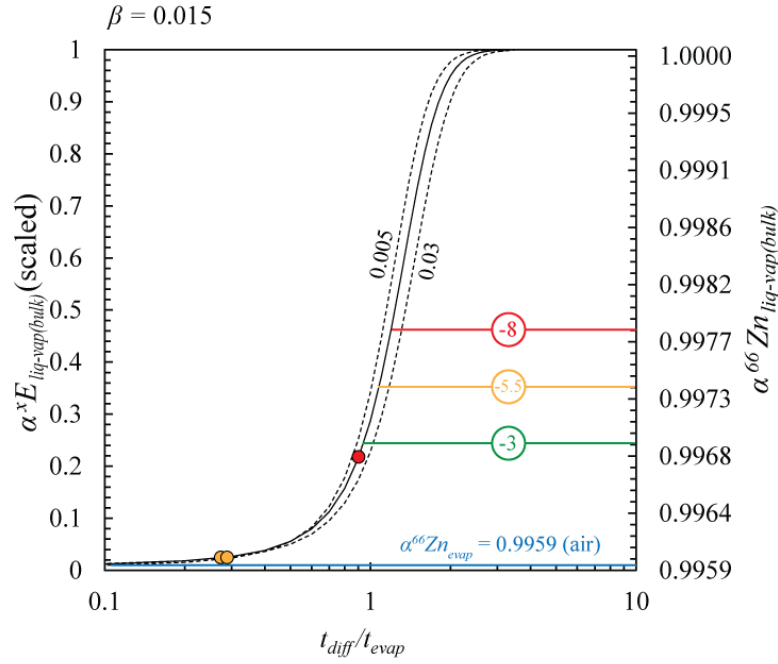
455 It is important to note that $(1-f(E)_{surf})$ is the fractional loss observed at the surface boundary layer, not
 456 that integrated throughout the entire bead. Whereas the diffusion timescale is given by (Crank, 1975):

$$457 \quad t_{diff} = \frac{1}{2} \frac{r^2}{D} (11)$$

458 With this in mind, t_{evap} is shown to be a factor of ~ 4 faster at $\log fO_2 = -8$ than at $\log fO_2 = -6$ (Table 2),
 459 giving rise to t_{diff}/t_{evap} of ~ 0.9 and ~ 0.28 , respectively. The effect of t_{diff}/t_{evap} on $^{i/j}E(\alpha_{vap-liq})_{bulk}$ follows a
 460 logistic function (Fig. 7), where, for $\beta = 0.015$:

$$461 \quad ^{i/j}E(\alpha_{vap-liq})_{bulk} = \frac{\left(1 - ^{i/j}E(\alpha_{vap-liq})_{surf}\right)}{1 + \exp\left(-3.85\left(\frac{t_{diff}}{t_{evap}} - 1.24\right)\right)} + ^{i/j}E(\alpha_{vap-liq})_{surf} (12)$$

462



463

464 **Figure 7.** The dependence of $^{ij}E(\alpha_{vap-liq})_{net}$ on the relative characteristic timescales of evaporation (t_{evap}) and
 465 diffusion (t_{diff}), assuming diffusion in the liquid is proportional to $(M_j/M_i)^\beta$, where $\beta = 0.015$ (solid line) and 0.005
 466 and 0.030 (dashed lines). Model results (eq. 12) for the predicted $^{ij}E(\alpha_{vap-liq})_{net}$ in experiments 26/12/18a-c
 467 (1300°C) are shown as yellow ($\log fO_2$ -6) and red ($\log fO_2$ -8) circles, assuming $^{ij}E(\alpha_{vap-liq})_{surf} = 0.9959$. The
 468 measured $^{ij}E(\alpha_{vap-liq})_{net}$ from other experimental runs at $\log fO_{2s}$ -0.68, -3, -5.5 and -8 (blue, green, yellow and red,
 469 respectively) are shown as horizontal lines.

470 The predicted increase in $^{ij}E(\alpha_{vap-liq})_{net}$ falls short of that measured (Fig. 5) for a given fO_2 , as shown by
 471 the horizontal lines on Fig. 7. Overlap between the red and yellow points with their respective coloured
 472 horizontal lines would constitute perfect agreement. However, given the uncertainties in the value of β
 473 and in the fractionation factor itself (especially considering the Cu and Zn isotope compositions of the
 474 zoned standalone samples were not determined), high t_{diff}/t_{evap} at lower fO_2 seems the most likely cause
 475 of increasing $^{ij}E(\alpha_{vap-liq})_{net}$ observed.

476

477 4.2. A general law for vaporisation

478 The Hertz-Knudsen-Langmuir (HKL) equation provides a quantitative means of assessing the
 479 mechanisms of elemental and isotopic fractionation due to evaporation that are observed
 480 experimentally. The degree to which gas molecules evaporating at the surface of a melt sphere
 481 equilibrate with the melt depends on the rate with which they are transported away from the surface,
 482 relative to the rate at which they are produced, a relationship described numerically;

$$483 \left(\frac{dn_i}{dt}\right)_{net} = -4\pi r^2 \frac{\gamma_{ev} p_{i,eq} - \gamma_{cn} p_{i,s}}{\sqrt{2\pi R M_i T}}. \quad (13)$$

484 Equation (13) states that the molar rate at which a species, i , in an ideal gas with a Maxwell-Boltzmann
 485 distribution of kinetic energies impinges upon a spherical surface is proportional to difference between
 486 the equilibrium partial pressure of that species ($p_{i,eq}$) and its actual pressure at the boundary layer of
 487 the evaporating surface, $p_{i,s}$, multiplied by their evaporation (γ_{ev}) and condensation (γ_{cn}) coefficients,
 488 respectively. Although the value of $p_{i,s}$ is not readily measured (*e.g.* by a probe that would itself perturb
 489 the boundary layer), it can be estimated by considering that, in a system with finite quantity of i , the net

490 production of gaseous molecules at the evaporating surface and their molar removal rate (mol/s) by
 491 mass transport must be equal, *i.e.*, $\left(\frac{dn_i}{dt}\right)_{net} = \left(\frac{dn_i}{dt}\right)_{trans}$, where $\left(\frac{dn_i}{dt}\right)_{trans}$ is given by (Bartlett, 1967):

$$492 \quad \left(\frac{dn_i}{dt}\right)_{trans} = -4\pi r^2 k_c \frac{(\gamma_{cn} p_{i,s} - p_{i,\infty})}{P} (1 - \exp(\xi) \operatorname{erfc}\sqrt{\xi}), \quad (14)$$

493 Here, $\xi = \frac{D_{ik} t}{2r^2}$, where D_{ik} the diffusion rate of species i through the gas otherwise composed of
 494 molecules with an average molar mass of k , r is the radius of the sphere, designates the approach to
 495 steady state conditions, which, in our experiments occurs after ~ 5 s ($\xi > 500$). At steady state, the mass
 496 transport rate is thus proportional to the partial pressure difference between $p_{i,s}$ and $p_{i,\infty}$ at an infinite
 497 distance from the boundary layer (taken here to be 0), related by the reciprocal total pressure (P) and
 498 the mass transfer coefficient, k_c . This quantity, which has units of mol/m².s, describes the facility with
 499 which mass is transported within a given medium, in this case, a flowing gas, and hence determines the
 500 thickness of the boundary layer surrounding the melt droplet.

501 The mass transfer coefficient is estimated through empirical correlations between dimensionless
 502 numbers determined under experimental conditions, and, for gases, is generally proportional to the
 503 diffusion rate raised to the power of 2/3 (Fuchs, 1959; Cussler, 2009). Expressions for k_c vary depending
 504 on whether the medium through which mass transfer occurs is subject to forced- or natural convection.
 505 The threshold between the two regimes is given by the ratio of the Grashof number¹ to the Reynolds
 506 number² squared, where values $\gg 1$ indicate natural convection, and those $\ll 1$ reflect forced
 507 convection. For forced convection, Frössling (1938) derived the following expression:

$$508 \quad k_c = \left(\frac{P}{RT}\right) \frac{D_{ik}}{r} \left(2 + 0.6 Re^{\frac{1}{2}} Sc^{\frac{1}{3}}\right), \quad (15)$$

509 Where Re is the Reynolds number and Sc is the Schmidt number³. Under natural convection conditions
 510 or for laminar flow ($Gr/Re^2 \gg 1$), as is the case for our experimental set-up (*Appendix B1*), the Chilton-
 511 Colburn equation (Chilton and Colburn, 1934; Wimber et al., 1977; Liu and Bautista, 1981), is suitable
 512 for calculating k_c :

$$513 \quad k_c = \frac{hP}{RT\rho C_p} \left(\frac{C_p \rho D_{ik}}{\kappa}\right)^{\frac{2}{3}}, \quad (16a)$$

$$514 \quad k_c = \left(\frac{P}{RT}\right) \frac{(D_{ik})^{\frac{2}{3}}}{r} \left(\left(\frac{\kappa}{\rho C_p}\right)^{\frac{1}{3}} + 0.3(U_\infty L)^{\frac{1}{2}} \left(\frac{\rho}{\eta}\right)^{\frac{1}{6}}\right) \quad (16b)$$

515 Where h is the heat transfer coefficient, U_∞ is velocity of the flowing gas at an infinite distance from
 516 the sample, L is the diameter of the tube, ρ is the density of the gas, η its viscosity, κ its thermal
 517 conductivity. Values and units for each term, and their meaning, are described in *Appendix B1*. The
 518 value of k_c is evaluated for the conditions of the furnace, at 1 bar both by direct measurement of h , 90
 519 W/m²K (Sossi et al. 2019) with eq. 16a, and by eq. 16b from the gas flow rate (0.025 m/s) and tube
 520 diameter (0.042 m), for which k_c values of 12.4 and 13.3 mol/m².s are obtained, respectively.

521 Recent studies (Richter et al., 2002; Young et al., 2019), have approximated k_c by assuming transport
 522 occurs purely by binary diffusion, and hence, in their analysis $k_c = \frac{D_{ik} P}{rRT}$, see also Craig (1968).
 523 Although our expression has a similar form, it differs in two principal ways; 1) it accounts for the
 524 advection and convection of the gas in the vicinity of the sample in accelerating mass transport (Stefan

¹ Grashof number, $Gr = g\rho^2\beta\Delta TL^3/\eta^2$, where g is the acceleration due to gravity, β is the coefficient of thermal expansion ($1/T$ for an ideal gas) and ΔT is the temperature difference between the sample surface and bulk gas.

² Reynolds number, $Re = U_\infty \rho L/\eta$.

³ Schmidt number, $Sc = \eta/D_{ik}\rho$.

525 flow) and 2) k_c is proportional to $(D_{ik})^{\frac{2}{3}}$ at the diffusive limit (where D_{ik} is small) and not D_{ik} . Under
 526 forced convection, the dependence of k_c on D_{ik} varies as a function of the Schmidt number, from a
 527 proportionality with $(D_{ik})^{\frac{2}{3}}$ at low Sc to one with D_{ik} at high Sc (eq. 15). The k_c calculated herein for
 528 natural convection is ~ 3 times faster than the diffusion-only value, ~ 3.8 mol/m².s.

529 Equating eq. (13) with eq. (14), and re-arranging, the unknown $p_{i,s}$ term is eliminated to obtain:

$$530 \left(\frac{dn_i}{dt}\right)_{net} = -4\pi r^2 \frac{\frac{\gamma_{i,ev} p_{i,eq}}{\sqrt{2\pi R M_i T}}}{1 + \frac{\gamma_{i,cn} P}{k_c \sqrt{2\pi R M_i T}} (1 - \exp(\xi) \operatorname{erfc}(\sqrt{\xi}))}. \quad (17)$$

531 As such, when mass transport is fast (*i.e.*, k_c is large), the denominator in eq. (17) tends to 1, and the
 532 net evaporation rate approaches the maximum evaporation rate ($p_{i,s} = 0$), given by the numerator. The
 533 value of $p_{i,eq}$ for any melt oxide species, $M^{x+n}O_{\frac{x+n}{2}}$, is given by its congruent evaporation:

$$534 M^{x+n}O_{\frac{x+n}{2}}(l) = M^x O_{\frac{x}{2}}(g) + \frac{n}{4} O_2(g) \quad (18)$$

535 where the equilibrium partial pressure of the stable gas species, $M^x O_{\frac{x}{2}}$, at the surface is:

$$536 p_{i,eq} = p \left(M^x O_{\frac{x}{2}} \right) = \frac{K_{(r)} X \left(M^{x+n} O_{\frac{x+n}{2}} \right) \gamma \left(M^{x+n} O_{\frac{x+n}{2}} \right)}{f(O_2)^{\frac{n}{4}}} \quad (19)$$

537 Where X is the mole fraction and γ the activity coefficient of $M^{x+n}O_{\frac{x+n}{2}}$ in the melt. Integrating with
 538 respect to time and concentration, following Sossi et al. (2019) (see their equations (2) to (8) for
 539 derivation), gives the analytical form of the equation:

$$540 \frac{X_i^t}{X_i^0} = \exp \left(- \frac{\frac{K_{(r)}^*}{f(O_2)^{n/4}} \frac{3M}{r\rho} \sqrt{\frac{1}{2\pi M_i RT}} (t-t_0)}{1 + \frac{\gamma_{i,cn} \rho C_P}{h} \left(\frac{\kappa}{C_P \rho D_{ik}} \right)^{\frac{2}{3}} \sqrt{\frac{RT}{2\pi M_i}} (1 - \exp(\xi) \operatorname{erfc}(\sqrt{\xi}))} \right) \quad (20)$$

541 Where $K_{(r)}^* = K_{(r)} \gamma \left(M^{x+n} O_{\frac{x+n}{2}} \right) \gamma_{i,ev}$. Evaluating the denominator with k_c calculated from eq. (16)
 542 for evaporation at 1 bar yields ~ 100 (dimensionless), which results in a flux that is therefore $\sim 10^2 \times$
 543 lower (*cf.* eq. 17) than for evaporation into a vacuum (for which the denominator is equal to unity), all
 544 else being equal. This factor was determined empirically when calculating K^* values in Sossi et al.
 545 (2019) and is predicted from first-principles herein.

546 Importantly, k_c is nearly independent of which element is being investigated, as it is determined
 547 primarily by the properties of the fluid medium surrounding the sample, and only mildly by those of
 548 the evaporating species themselves, *via* the D_{ik} term (*cf.* eqs. 15, 16). Furthermore, k_c does not change
 549 significantly as a function of fO_2 , nor for different gas flow rates (provided flow remains laminar). This
 550 expectation is confirmed in tests with two different flow rates at 1500 °C (P31/07/18a and b; 200 ml/min
 551 and 20 ml/min, respectively) and 1400 °C (P01/08/18a and b; 200 ml/min and 20 ml/min, respectively)
 552 each using pure CO₂, in which the fractional vapour loss was within uncertainty of unity (Table 1). The
 553 same is true of samples run in air compared to those run in a flowing gas, k_c varies from 13.3 mol/m².s
 554 with $U = 0.025$ m/s to 11.1 mol/m².s with no gas flow.

555 Compared with elemental loss, predicting isotopic fractionation is comparatively simpler, because the
 556 global variables cancel when taking the ratio of fluxes of two isotopes. Isotopic fractionation is
 557 calculated as:

$${}^{i/j}E(\alpha_{vap-liq})_{net} = -4\pi r^2 \frac{\frac{\gamma_{i,ev} p_{i,eq}}{\sqrt{2\pi R M_i T}}}{1 + \frac{\gamma_{i,cn} P}{k_{c,i} \sqrt{2\pi R M_i T}} (1 - \exp(\xi) \operatorname{erfc} \sqrt{\xi})} / -4\pi r^2 \frac{\frac{\gamma_{j,ev} p_{j,eq}}{\sqrt{2\pi R M_j T}}}{1 + \frac{\gamma_{j,cn} P}{k_{c,j} \sqrt{2\pi R M_j T}} (1 - \exp(\xi) \operatorname{erfc} \sqrt{\xi})} \quad (21)$$

559 This equation can be simplified considering that the denominator is related to the ratio of $p_{i,s}$ and $p_{i,eq}$
 560 by equations (13) and (14) and simplifying:

$$561 \quad 1 - \frac{1}{1 + \frac{\gamma_{i,cn} P}{k_c \sqrt{2\pi R M T}} (1 - \exp(\xi) \operatorname{erfc} \sqrt{\xi})} = \left(\frac{p_{i,s}}{p_{i,eq}} \right) \quad (22)$$

562 Therefore, simplifying eq. (21) and substituting in eq. (22), one obtains:

$$563 \quad {}^{i/j}E(\alpha_{vap-liq})_{net} = \frac{\gamma_{i,ev} p_{i,eq}}{\gamma_{j,ev} p_{j,eq}} \sqrt{\frac{M_j \left(1 + \frac{\gamma_{j,cn} P}{k_{c,j} \sqrt{2\pi R M_j T}} \right)}{M_i \left(1 + \frac{\gamma_{i,cn} P}{k_{c,i} \sqrt{2\pi R M_i T}} \right)}} = \frac{\gamma_{i,ev} p_{i,eq}}{\gamma_{j,ev} p_{j,eq}} \sqrt{\frac{M_j \left(1 - \frac{p_{i,s}}{p_{i,eq}} \right)}{M_i \left(1 - \frac{p_{j,s}}{p_{j,eq}} \right)}} \quad (23)$$

564 Which is applicable to evaporation in a steady-state, open system for any pressure and gas flow regime.
 565 When transport is sufficiently fast that $p_{i,s}/p_{i,eq} \rightarrow 0$, then ${}^{i/j}E(\alpha_{vap-liq})_{net} \rightarrow (M_j/M_i)^{0.5}$. The inverse case
 566 occurs when transport is slow relative to evaporation such that $p_{i,s}/p_{i,eq} \rightarrow 1$. Thus, when taking the ratio
 567 of the fluxes of two isotopes (eq. 21), all terms become small with respect to $1/k_c$ to give:

$$568 \quad {}^{i/j}E(\alpha_{vap-liq})_{net} (D_{ik} \rightarrow 0) = \frac{\frac{\gamma_{j,cn} \rho C_P \left(\frac{\kappa}{C_P \rho D_{jk}} \right)^{\frac{2}{3}}}{h}}{\frac{\gamma_{i,cn} \rho C_P \left(\frac{\kappa}{C_P \rho D_{ik}} \right)^{\frac{2}{3}}}{h}} = \frac{\gamma_{j,cn}}{\gamma_{i,cn}} \left(\frac{D_{ik}}{D_{jk}} \right)^{\frac{2}{3}} = \frac{\gamma_{i,cn}}{\gamma_{j,cn}} \left(\frac{\mu_{jk}}{\mu_{ik}} \right)^{\frac{1}{3}} \quad (24)$$

569 Where $\mu_{ik} = \frac{m_i m_k}{m_i + m_k}$, the reduced mass of i and k . Since, save for D_{ik} , all terms that determine k_c are
 570 properties of the gas phase in which evaporation occurs (*i.e.*, they are independent of isotopic mass)
 571 they also cancel. This assumption holds provided the evaporating species are dilute enough that they do
 572 not themselves influence the properties of the gas medium k . Then, because D_{ik} is itself proportional to
 573 the inverse square root of the reduced mass $(\mu_{ik})^{-\frac{1}{2}}$ (eq. B6), ${}^{i/j}E(\alpha_{vap-liq})_{net}$ is proportional to $(\mu_{jk}/\mu_{ik})^{1/3}$
 574 at the diffusive limit (*i.e.*, when diffusion through the gas is the rate-limiting step for mass transfer of
 575 the evaporating species away from the evaporating surface).

576 At the high-temperatures relevant to these experiments, quantum contributions (*e.g.* vibrational
 577 frequency) to the free energy change of the isotopic substitution are insignificant relative to the thermal
 578 energy of the system ($3/2 k_B T$, $k_B =$ Boltzmann's constant) such that they can be ignored. Thus, we make
 579 the assumption that $p_{i,eq} = p_{j,eq}$. Similarly, we assume that both the evaporation and condensation
 580 coefficients are unity for liquids (see Sossi and Fegley, 2018 and Shornikov, 2015 for discussions).
 581 Evaluating the denominator of the left-hand side of eq. (22) for evaporation experiments at 1 bar (\sim
 582 100), one finds that $p_{i,s}/p_{i,eq} \approx 0.99$. In detail, this value varies according to the molar mass of the
 583 evaporating species, because k_c and M depend on the precise mass of the isotope considered. Thus,
 584 using eq. (22), the values of $\frac{p_{i,s}}{p_{i,eq}}$ and $\frac{p_{j,s}}{p_{j,eq}}$ obtained for the mass pairs ${}^{65}\text{Cu}$ - ${}^{63}\text{Cu}$ and ${}^{66}\text{Zn}$ - ${}^{64}\text{Zn}$, (where
 585 $i = {}^{66}\text{Zn}$ or ${}^{65}\text{Cu}$ and $j = {}^{64}\text{Zn}$ or ${}^{63}\text{Cu}$) are substituted into eq. (23) and show that ${}^{i/j}E(\alpha_{vap-liq})_{net}$ approaches
 586 $(D_{ik}/D_{jk})^{2/3}$, the diffusive limit (as D_{ik} tends to 0), which is 0.9966 in air or 0.9958 in pure CO_2 for both
 587 ${}^{66/64}\text{Zn}$ and ${}^{65/63}\text{Cu}$. These calculations overlap with the values observed in samples for which elemental
 588 zoning in the condensed phase is absent (as informed from analogue experiments, Sossi et al., 2019);
 589 0.9959 ± 0.0002 for ${}^{66/64}\text{Zn}$ and 0.9972 ± 0.0001 for ${}^{65/63}\text{Cu}$.

590 For Cu, whether the experiments were performed in air or CO-CO_2 mixtures, the isotopic fractionation
 591 factor remains constant, whereas eq. 24 would predict a decrease in ${}^{i/j}E(\alpha_{vap-liq})$ (*i.e.*, more fractionation)
 592 as the molar mass of the gas phase increases from air (0.029 kg/mol) to CO_2 (0.044 kg/mol). We also

593 note that slight deviations from unity are permitted for $\frac{\gamma_{i,ev}}{\gamma_{j,ev}}$ and $\frac{p_{i,eq}}{p_{j,eq}}$. For a monatomic gas, $\frac{p_{i,eq}}{p_{j,eq}}$ must
594 be < 1 , as the heavier isotope (i) will have a slightly lower equilibrium partial pressure than the lighter
595 isotope (j). The same is true for $\frac{\gamma_{i,ev}}{\gamma_{j,ev}}$ because the value of $\gamma_{i,ev}$ relates to vibrational frequencies (Knacke
596 and Stranski, 1952; Penner, 1952; Ackermann et al., 1962) making it difficult to envisage any kinetic
597 mechanism that would favour detachment of the heavier isotope over the lighter isotope of the same
598 chemical species. Both processes will decrease $^{i/j}E(\alpha_{liq-vap})$ (more fractionation) compared to those
599 calculated from eq. 23 assuming $\frac{\gamma_{i,ev}p_{i,eq}}{\gamma_{j,ev}p_{j,eq}} = 1$. For example, given $^{66/64}\alpha_{Zn(g)-ZnO(s)} = \frac{p_{66,eq}}{p_{64,eq}} = 0.99985$ from
600 Ducher et al. (2016) at 1573 K, a value of $\frac{\gamma_{66,ev}}{\gamma_{64,ev}} = 0.9995$ would be required to give $^{66/64}Zn(\alpha_{vap-liq}) =$
601 0.9959 . However, given the complexity of predicting the value of k_c in real systems together with
602 possible small variations in $\frac{\gamma_{i,ev}}{\gamma_{j,ev}}$ and $\frac{p_{i,eq}}{p_{j,eq}}$ and in the experimental conditions, we consider that the
603 experimental values are satisfactorily reproduced by the model. It therefore also illustrates that the
604 assumption of the ratios of evaporation coefficients of two isotopes of a given species being equal to
605 unity is well-founded.

606

607 **5.0. Implications**

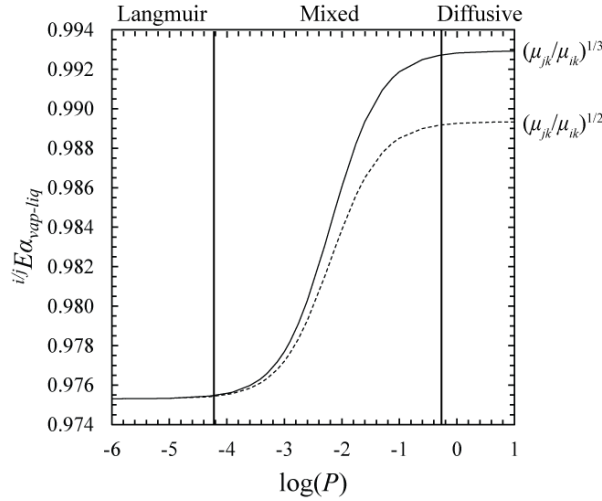
608

609 *5.1. Comparison with experimental data*

610 Although vaporisation studies have typically sought to explain the cosmochemical features of Calcium-
611 Aluminium-rich Inclusions (CAIs) or chondrules, and have thus been performed at very low pressure
612 (vacuum) conditions (Wang et al., 2001; Richter et al., 2002; Yu et al., 2003; Janney et al., 2004;
613 Wombacher et al., 2004; Dauphas et al., 2004; Richter et al., 2007; Knight et al., 2009; Mendybaev et
614 al., 2017), an increasing number of studies have turned to volatilisation experiments at 1 bar (Yu et al.,
615 2003; Richter et al., 2011; Wimpenny et al., 2019) in order to understand the origin of the limited
616 isotopic fractionation observed in planetary materials.

617 The formalism developed in section 4.2. permits enumeration of the effect of total pressure on the
618 vapour-liquid fractionation factor. Higher total pressures cause a linear decrease in both the diffusion
619 coefficient, D_{ik} (eq. B6) and in the density of the ambient gas (eq. B2). The net effect is to decrease the
620 mean free path of evaporating molecules, thereby depressing the evaporation rate indirectly through the
621 build-up of molecules (higher $\frac{p_{i,s}}{p_{i,eq}}$) in the gaseous boundary layer surrounding the melt sphere. Because

622 the mass transfer coefficient, k_c , is proportional to $(D_{ik})^{\frac{2}{3}}$, which is itself proportional to $1/P$, and $\rho^{-1/3}$,
623 which is itself proportional to P (cf. eq. 16), k_c varies with $1/P$. This dependence mirrors that predicted
624 from the diffusion-only mass transfer coefficient, for which k_c is proportional to D_{ik} (e.g., Richter et al.,
625 2002).



626

627 **Figure 8.** The effect of pressure, expressed as $\log(P)$ (with P in bars) on the vapour-liquid isotopic fractionation
 628 factor, ${}^{i,j}E(\alpha_{\text{vap-liq}})_{\text{net}}$. Here, $i = {}^{41}\text{K}$ and $j = {}^{39}\text{K}$, and the mass transfer coefficient is calculated at $1450\text{ }^\circ\text{C}$ for natural
 629 convection in air (k), $M_k = 0.029\text{ kg/mol}$. The fractionation factor is then calculated according to the dependence
 630 on $(D_{ik}/D_{jk})^{2/3}$ (solid line) and (D_{ik}/D_{jk}) (dashed line), where the value of the mass transfer coefficient is otherwise
 631 constant. Solid vertical lines delineate the fields of Langmuir evaporation ($p_{i,s}/p_{i,eq} < 0.01$) and the diffusion-
 632 limited regime ($p_{i,s}/p_{i,eq} > 0.99$) with the intervening pressure range giving rise to a ‘mixed’ evaporative regime.
 633 Lighter ambient gases (k) will shift these curves to the left and to a higher diffusion-limited ceiling, and vice-
 634 versa.

635 Calculation of ${}^{41}\text{K}/{}^{39}\text{K}(\alpha_{\text{vap-liq}})_{\text{net}}$ from 10 bar to 10^{-6} bar at $1450\text{ }^\circ\text{C}$ for a gas with mean molar mass of
 636 0.029 kg/mol indicates that the diffusive limit (defined as $p_{i,s}/p_{i,eq} > 0.99$) occurs above $\sim 0.5\text{ bar}$,
 637 whereas pure Langmuir vaporisation (when $p_{i,s}/p_{i,eq} < 0.01$) is expected below $\sim 10^{-4}\text{ bar}$ (Fig. 8). High-
 638 precision evaporation experiments over a range of pressures are required in order to verify these
 639 predictions. Note that, because this treatment assumes steady-state loss (*cf.* eq. 14), the fractionation
 640 factor tends to the diffusion-limited value (~ 0.993 in air for ${}^{41}/{}^{39}\text{K}$), rather than to the equilibrium
 641 fractionation factor (~ 1). The latter would be applicable as an upper limit to cases in which the gas
 642 remains in contact with the condensed phase (*i.e.*, a closed system) at any pressure.

643 At the diffusive limit, as is relevant for evaporation at 1 bar , our expression predicts a fractionation
 644 factor that is proportional to $(\mu_{jk}/\mu_{ik})^{1/3}$ (eq. 24). However, because Richter et al. (2002) and Young et
 645 al. (2019) assume that k_c depends simply on D_{ik} , these studies predicted that ${}^{i,j}E(\alpha_{\text{vap-liq}})_{\text{net}}$ tends to
 646 $(\mu_{jk}/\mu_{ik})^{1/2}$. To ground-truth these different dependencies, we summarise existing experimental data for
 647 the isotope fractionation of moderately volatile elements during their vaporisation from silicate melts
 648 at 1 bar in Table 3 and Fig. 9. These experiments were all performed under low flow rates that permits
 649 application of eq. (16) in the limit D_{ik} tends to 0. Increasingly higher flow rates would accelerate mass
 650 transfer, with the net effect of decreasing $p_{i,s}/p_{i,eq}$, and thus ${}^{i,j}E(\alpha_{\text{vap-liq}})_{\text{net}}$ (*i.e.*, more fractionation) relative
 651 to the $p_{i,s}/p_{i,eq} = 1$ limit.

652

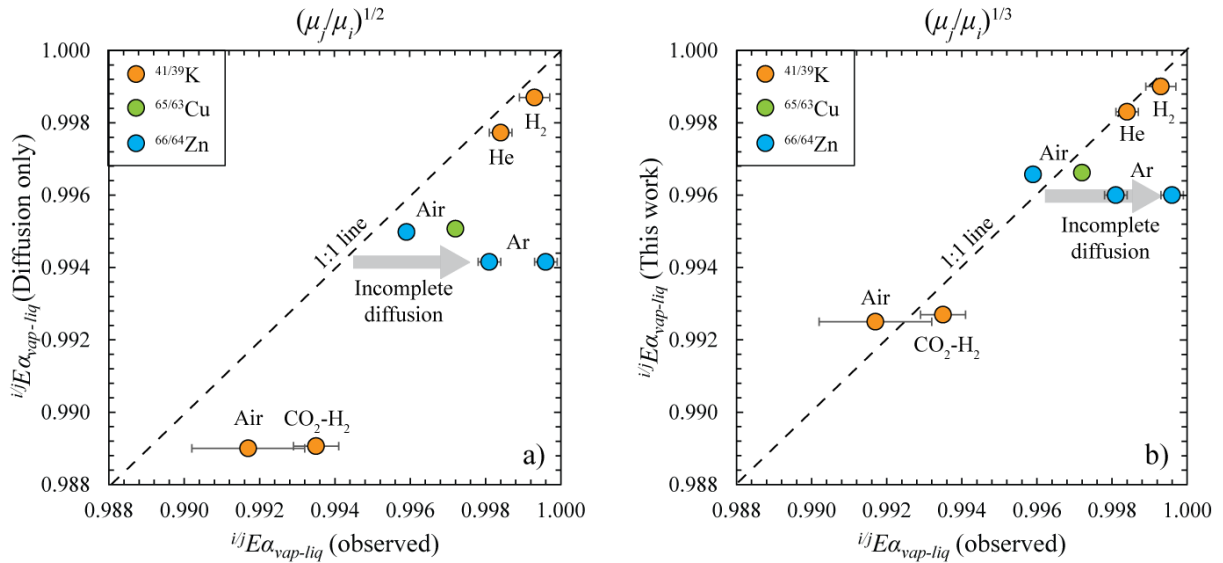
Table 3. Isotopic fractionation of moderately volatile elements during their evaporation from silicate melts at a total pressure of 1 bar .

Element	Isotope Ratio	Gas medium	$\log f\text{O}_2$	Temperature ($^\circ\text{C}$)	Material	${}^{i,j}E(\alpha_{\text{vap-liq}})_{\text{net}}$ Diffusion only	${}^{i,j}E(\alpha_{\text{vap-liq}})_{\text{net}}$ This work	${}^{i,j}E(\alpha_{\text{vap-liq}})_{\text{net}}$ Observed	Ref.
K	41/39	Air	-0.68	1450	IIAB Chondrule	0.9890	0.9925	0.9917 ± 0.0015	Y+ 03
K	41/39	$\text{CO}_2\text{-H}_2$	-6.93	1430	IIAB Chondrule	0.9891	0.9927	0.9935 ± 0.0006	R+ 11
K	41/39	H_2	-	1450	IIAB Chondrule (K-rich, Fe-free)	0.9987	0.9990	0.9993 ± 0.0004	R+ 11

K	41/39	He	-	1450	IIAB Chondrule (K-rich, Fe-free)	0.9977	0.9983	0.9984 ± 0.0003	R+ ¹¹
Zn	66/64	Ar	-	1600 - 2200	Arkosic soil	0.9942	0.9960	0.9996 ± 0.0003	W+ ¹⁹
Zn	66/64	Ar	-	1600 - 2200	Rhyolitic soil	0.9942	0.9960	0.9981 ± 0.0003	W+ ¹⁹
This work									
Cu	65/63	Air, CO ₂	-0.68, -3, -5.5	1300 - 1500	Ferrobasalt	0.9950	0.9966	0.9972 ± 0.0001	
Zn	66/64	Air	-0.68	1300 - 1500	Ferrobasalt	0.9951	0.9966	0.9959 ± 0.0002	

Y+⁰³ = Yu et al. (2003); R+¹¹ = Richter et al. (2011); W+¹⁹ = Wimpenny et al. (2019)

653



654

655 **Figure 9.** A comparison between the isotopic fractionation factor between vapour and liquid, $^{ij}E(\alpha_{vap-liq})_{net}$,
656 observed in experimental studies of the evaporation of $^{41/39}\text{K}$ (orange), $^{65/63}\text{Cu}$ (green) and $^{66/64}\text{Zn}$ (blue) from
657 silicate melts at 1 bar and a variety of gas mixtures (labelled next to points), compared to that predicted according
658 to **a)** a $(\mu_{jk}/\mu_{ik})^{1/2}$ dependence and **b)** a $(\mu_{jk}/\mu_{ik})^{1/3}$ dependence on mass transport through the gas phase. The dashed
659 1:1 line denotes perfect agreement between experiment and theory.

660 Although both expressions correctly predict the sense of isotopic fractionation, expressions with a
661 $(\mu_{jk}/\mu_{ik})^{1/2}$ dependence underestimate the value of $^{ij}E(\alpha_{vap-liq})_{net}$ (Fig. 9a), whereas the $(\mu_{jk}/\mu_{ik})^{1/3}$
662 proportionality derived herein (*Appendix B1*) lies within ± 0.0005 of the experimental data (Fig. 9b).
663 Experiments over a wide range of gas mixtures and isotopic systems therefore empirically verify the
664 dependence on $(\mu_{jk}/\mu_{ik})^{1/3}$. This new formalism also ameliorates the difficulty of having to account for
665 fractionation factors that are smaller (i.e., higher $^{ij}E(\alpha_{vap-liq})_{net}$) than predicted by the $(\mu_{jk}/\mu_{ik})^{1/2}$
666 dependence, as is the case for almost all isotopic systems investigated (Fig. 9a). Values of $^{ij}E(\alpha_{vap-liq})_{net}$
667 that exceed the diffusion-limited value require either that *i)* $p_{i,eq} > p_{j,eq}$ and/or *ii)* $\gamma_{i,ev} > \gamma_{j,ev}$; both of which
668 are equally unphysical (*section 4.2.*). The departure to higher values of $^{ij}E(\alpha_{vap-liq})_{net}$ observed in some
669 vacuum experiments (particularly for $^{25/24}\text{Mg}$; Richter et al. 2007; Mendybaev et al. 2017) may relate
670 to different evaporation coefficients among *different species*. That is, that $\gamma_{\text{MgO}}/\gamma_{\text{Mg}} > 1$, such that
671 there is more $\text{MgO}(\text{g})$ relative to $\text{Mg}(\text{g})$ than expected under equilibrium conditions, meaning the mean
672 molar mass of Mg in the gas phase increases. A detailed exploration of such a hypothesis is beyond the
673 scope of this work.

674 Conspicuous in Fig. 9 are the $^{66/64}\text{Zn}(\alpha_{vap-liq})$ fractionation factors of Wimpenny et al. (2019), which fall
675 to slightly (rhyolitic soil) or significantly (arkosic soil) higher values. Notably, the experimental charges
676 at temperatures below 1800 °C were not fully molten, as attested to by their non-aerodynamic forms,
677 making it difficult to quantify evaporation rates thermodynamically. Moreover, all other variables being

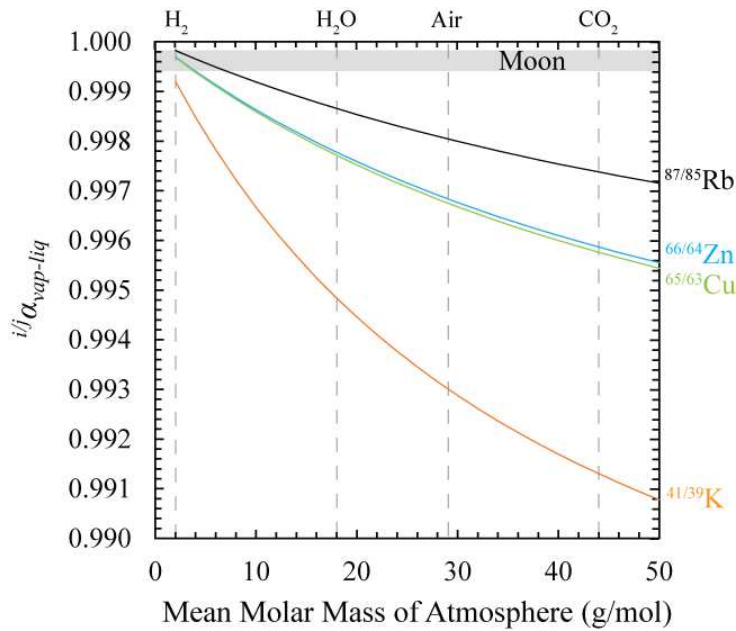
678 held constant, the amount of Zn remaining in the melt does not decrease as a function of time (for runs
679 < 60 s) as would be expected from eq. 6. This suggests evaporation did not reach a steady state until ~
680 60 s. Indeed, arkosic soil shows a variation of $^{66/64}\text{Zn}(\alpha_{\text{vap-liq}})$ with run time. After 60 s, the vaporisation
681 rate can be modelled with a $\log K^*_{\text{Zn}}$ value of -3.75 ± 0.29 at all temperatures for both the arkosic and
682 rhyolitic soil, which is lower (slower evaporation rate) than predicted from extrapolation of the trends
683 shown in Fig. 3. The rhyolitic soil shows no dependence of $^{66/64}\text{Zn}(\alpha_{\text{vap-liq}})$ on experimental run time,
684 and is also much closer to the predicted value in pure Ar, 0.9960.

685 Because both compositions have > 70% SiO₂ by definition (and likely >90% in the case of arkose) and
686 the experiments were performed at 1 bar where water solubility is low (< 0.1 wt. %; Dixon et al., 1995),
687 the melt viscosity in both cases is likely to be of the order of $\log \eta \approx 3$ to 4 at 2000 °C (Stevenson et al.,
688 1998; Giordano et al., 2008); at least $10^3 \times$ more viscous than the melt compositions used herein,
689 meaning diffusion rates of Zn were also $10^3 \times$ slower. A quantitative model of vaporisation rate for the
690 experiments of Wimpenny et al. (2019) cannot be constructed because they were not $f\text{O}_2$ -buffered, nor
691 were zoning profiles across the glass beads measured. However, the empirical observation that
692 $^{66/64}\text{Zn}(\alpha_{\text{vap-liq}})$ in their experiments are higher than *i*) predicted for a diffusive-limited gas regime (Fig.
693 9b) and *ii*) observed for ferrobaltic melts in which no diffusion profiles are present (Fig. 5b), strongly
694 suggests the influence of incomplete diffusion to the evaporating surface in increasing $^{66/64}\text{Zn}(\alpha_{\text{vap-liq}})$
695 during evaporation from rhyolitic and particularly arkosic melts.

696
697

5.2. Evaporation processes in natural rocks

698 The corollary that the rate of mass transfer of two isotopes from the evaporation surface is proportional
699 to the ratios of the reduced masses of the evaporating species, $(\mu_{jk}/\mu_{ik})^{1/3}$, is that fractionation factors at
700 the diffusive limit are sensitive to the mean molecular mass of the surrounding gas. In detail, isotopic
701 fractionation is suppressed if diffusion occurs through lighter gases, and promoted for diffusion through
702 heavier gases. Physically, this phenomenon arises because, when the difference in molar mass between
703 two constituents is large, the collisions between the lighter molecules in a binary gas mixture govern its
704 velocity distribution (Chapman and Cowling, 1970). This can be verified mathematically, where the
705 reduced mass tends to that of the lighter constituent as the mass difference between the two increases,
706 independent of their abundance ratio. In our case, as the lighter, ambient gas (*k*) is in excess of both
707 evaporating species, *i* and *j* (the so-called quasi-Lorentzian condition; Mason, 1957), then, the greater
708 the difference between m_k and $m_{i,j}$, the more the reduced masses μ_{jk} and μ_{ik} tend to a common value (m_k),
709 and hence the closer the fractionation factor is to unity. Conversely, if $m_k \gg m_{i,j}$, then the reduced mass
710 of the mixture *ik* is approximated by m_i (and the mixture *jk* by m_j), and the fractionation factor
711 approaches $(m_j/m_i)^{1/3}$. Figure 10 illustrates the dependence of $^{i/j}\text{E}(\alpha_{\text{vap-liq}})_{\text{net}}$ on the atmospheric molar
712 mass (m_k) at the diffusive limit for four moderately volatile element isotope pairs.



713

714 **Figure 10.** The modelled change of $i/j(\alpha_{\text{vap-liq}})_{\text{net}}$ at the diffusive limit for four moderately volatile element
 715 isotope pairs ($^{87/85}\text{Rb}$, black; $^{66/64}\text{Zn}$, blue; $^{65/63}\text{Cu}$, green; $^{41/39}\text{K}$, orange) evaporating as monatomic gases, as a
 716 function of the mean molar mass of the gas through which they diffuse. Common molecules or atmospheres to
 717 which these molar masses correspond are shown as dashed grey lines. The grey horizontal bar corresponds to
 718 $i/j(\alpha_{\text{vap-liq}})_{\text{net}}$ inferred for the Moon, deduced from the isotopic compositions of lunar mare basalts. In each case,
 719 the fractionation factor lies between 0.9994 and 0.9999 (see text).

720

5.2.1. Tektites

721 Samples for which the composition and total pressure of the atmosphere into which evaporation occurs
 722 is known presents the simplest scenario to understand the conditions of vaporisation in natural systems.
 723 This criterion is satisfied by tektites, glasses that formed upon melting and subsequent quenching of
 724 crustal rocks during hypervelocity impact events (Koeberl, 1986 and references therein). Because these
 725 events are recent (<35 Myr; Koeberl, 1994) up to ~790,000 years ago for Australites (Schneider et al.,
 726 1992), evaporation occurred into air with characteristics identical to those observed today.

727 The derivation of $i/j(\alpha_{\text{vap-liq}})_{\text{net}}$ from analyses of tektites is sensitive to the assumed composition of their
 728 source rocks. Although the Cu and Zn isotope composition of the continental crust is not expected to
 729 differ significantly from igneous rocks (at least on the scale relative to the fractionation observed in
 730 tektites), their initial concentrations may vary by more than a factor of 2 (Taylor and Kaye, 1969;
 731 Koeberl, 1986; Žák et al., 2016). Owing to the compositional similarity borne by non-volatile elements
 732 in tektites to the upper continental crust (UCC), it has been customary to use it to calculate Cu_0 and Zn_0
 733 which yields 28 ppm and 67 ppm, respectively (Rudnick and Gao, 2003). However, source
 734 compositions among tektite groups may vary, as substantiated by the non-linear arrays in $\ln f(\text{E})$ vs. $\delta^i\text{E}$
 735 space (Moynier et al., 2009; Jiang et al., 2019), complicating the extraction of accurate $i/j(\alpha_{\text{vap-liq}})_{\text{net}}$
 736 from these data.

737 Considering these uncertainties, both $^{66/64}\text{Zn}(\alpha_{\text{vap-liq}})$ and $^{65/63}\text{Cu}(\alpha_{\text{vap-liq}})$ lie in the range 0.996 to 0.999
 738 (Moynier et al., 2009; Rodovska et al., 2017; Jiang et al., 2019), values which are broadly consistent
 739 with those predicted from our model (0.9966). The smaller fractionation of $^{66/64}\text{Zn}(\alpha_{\text{vap-liq}})$ with respect
 740 to $^{65/63}\text{Cu}(\alpha_{\text{vap-liq}})$ inferred by Moynier et al., (2010) was attributed to the slower diffusion of Zn in the
 741 tektite melt at high temperatures with respect to Cu. On the other hand, a recent measurement of and
 742 elemental profiles of Cu, Zn and K in a tektite from Hainan did not observe systematic zoning in
 743 abundance for any of the three elements. Nevertheless, the absence of zoning in the Hainan tektite ($r =$
 744 0.045 m) does not necessarily exclude diffusion-limited fractionation in other tektites, as they are each

745 sensitive to the local formation conditions and may have also re-homogenised by convection during- or
746 post-vaporisation. Our expression predicts no dependence of $t_{\text{evap}}/t_{\text{diff}}$ on r for diffusion-limited
747 conditions, meaning zoning is as likely to manifest itself in small tektites as it is in larger ones. That K
748 isotopes do not show any measurable fractionation in tektites (Jiang et al., 2019), despite the high
749 diffusion coefficient of K in silicate melts (Jambon, 1982) relative to Zn, instead suggests that potassium
750 remained non-volatile; a loss of $\sim 1\%$ of its initial budget with $^{41/39}\text{K}(\alpha_{\text{vap-liq}}) = 0.993$ would result in
751 isotopic fractionation of $+0.07\%$. Its lack of evaporative loss is plausibly related to its very low activity
752 coefficient in silicate melts, $\sim 10^{-4}$ (Sossi et al., 2019), and in particular those that are silica-rich (Borisov,
753 2009), causing a $10,000\times$ decrease in partial pressure relative to cases in which K behaves ideally. As
754 such, much of the K remains in the melt, even for considerable losses of Cu and Zn.

755 Our experiments demonstrate that $^{66/64}\text{Zn}(\alpha_{\text{vap-liq}})$ is slightly lower (more fractionation) than $^{65/63}\text{Cu}(\alpha_{\text{vap-}}$
756 $\text{liq})$ when the glass is homogeneous, opposite to that observed in tektites. This discrepancy is most readily
757 explicable by diffusion-limited Zn isotope fractionation during evaporation due to its slower diffusion
758 through the tektite liquid relative to Cu, as verified experimentally in Fig. 5, and modelled in section
759 4.1 and in Moynier et al. (2009). Indeed, core and rim analyses of a single Australite tektite (Moynier
760 et al., 2009) show that the core is enriched in Zn (265 ppm) and light isotopes ($\delta^{66}\text{Zn} = +1.22\%$) relative
761 to the rim (19 ppm and $+1.83\%$), in qualitative agreement with such a scenario. On the basis that Sn
762 isotopes, with a similar relative mass difference, show comparable isotopic fractionation to Zn (and
763 thus less than Cu) in the same tektites also lends support a diffusive barrier to isotope fractionation
764 during evaporation (Creech et al., 2019).

765 It remains challenging to use experimental results in a uniform temperature environment to
766 quantitatively assess isotopic fractionation in tektites. This is because, in the impact scenario that forms
767 tektites, shocked material follows a Hugoniot before undergoing decompression that leads to
768 fragmentation in which material intersects the liquid-vapour phase transition from the liquid side
769 (Melosh and Vickery, 1991), meaning temperature cannot be assumed to be constant over the
770 vaporisation timescale and steady-state conditions may have not been achieved (Humayun and Koeberl,
771 2004). Some authors have also appealed to a vapour-cloud produced by the impact itself in modifying
772 the local atmospheric conditions around tektite precursors undergoing fusion and vaporisation
773 (Rodovska et al. 2017). Further work is required to evaluate the degree and sense of internal elemental
774 and isotope zonation within tektite glasses, together with a better estimate of their initial abundances in
775 potential source rocks (e.g. Zak et al. 2016) to discriminate between the mechanisms of vaporisation
776 during their formation.

777 5.2.2. The Moon

778 Assessment of the volatile loss that was thought to have affected the composition of the Moon following
779 a giant impact event is subject to the opposite problem; although the fractionation factors for moderately
780 volatile elements are well-defined, the composition of its likely atmosphere or the locus of volatile
781 depletion are not. The separation of condensed phases from gas may have occurred during various
782 stages of lunar formation, such as upon viscous spreading attending proto-lunar disk collapse (Canup
783 et al. 2015), partial condensation during cooling of a synestia (Lock et al. 2018), or loss of an
784 atmosphere in equilibrium with an early lunar magma ocean (Sossi et al. 2018; Charnoz et al. 2019).
785 The bulk composition of the atmosphere at the vapour-liquid interface in each scenario, and the
786 mechanisms by which volatiles are lost, are poorly constrained and are expected to have varied
787 according to the local physico-chemical conditions. Stable isotopes may shed light on these issues, as
788 their fractionation is sensitive to both the mode of evaporative loss and transport (sections 4.1, 4.2) and
789 the thermodynamic conditions (section 3.2) under which volatile depletion took place.

790 The $^{ij}\text{E}(\alpha_{\text{vap-liq}})_{\text{net}}$ inferred for the Moon is calculated on the basis of the elemental and isotopic
791 compositions of lunar mare basalts, the most extensive form of magmatism exposed on the lunar surface
792 (BVSP, 1981), which have subsequently been used to inform compositional models for the bulk Moon

793 (O'Neill, 1991; Taylor and Wieczorek, 2014; Ni et al., 2019). Although lunar pyroclastic glass beads
794 have also been used for this purpose (Hauri et al., 2015; Ni et al., 2019), their utility is limited in this
795 context because recondensation occurring during fire-fountaining has resulted in isotopic fractionation,
796 overprinting the primary mantle signature (Moynier et al., 2006; Herzog et al., 2009). Mg Suite rocks,
797 due to their high Mg#, pristine nature and old crystallisation ages are also useful probes of lunar interior
798 composition (Warren, 2005; Shearer et al., 2015). Mg Suite cumulates have lower Zn contents and are
799 more isotopically fractionated than mare basalts, with the net result being the inferred $^{66/64}\text{Zn}(\alpha_{\text{vap-liq}})$ is
800 comparable (~ 0.9993) to that defined by mare basalts (0.9996) (see Day et al., 2020).

801 As such, the definition of a bulk lunar mantle is a conceptual construct, akin to the 'bulk silicate Earth',
802 and should not be taken to imply that the lunar interior is homogeneous. Rather, we examine rocks of
803 the same lithology (*i.e.*, mare basalts) for which compositional and isotopic variations are statistically
804 similar within a given group such that they permit comparison among different elements. Then, given
805 the isotopic and chemical similarity observed for non-volatile elements between the Earth's mantle and
806 the lunar mantle (Warren, 2005; Zhang et al., 2012; Young et al., 2016; Sossi and Moynier, 2017;
807 Sedaghatpour and Jacobsen, 2019), the Cu and Zn elemental and isotope compositions of the bulk
808 silicate Earth are adopted as the compositional starting points from which lunar volatile loss is modelled.
809 Here we investigate the $^{i/j}\text{E}(\alpha_{\text{vap-liq}})$ of four moderately volatile elements, K, Cu, Zn and Rb, for which
810 both the isotopic and chemical composition in the lunar mantle is well constrained, as summarised in
811 Table 4.

Table 4. A summary of the Zn, Cu, K and Rb abundances and isotopic compositions in the Earth's and Moon's mantle (based on mare basalts), and calculated vapour-Moon fractionation factors.

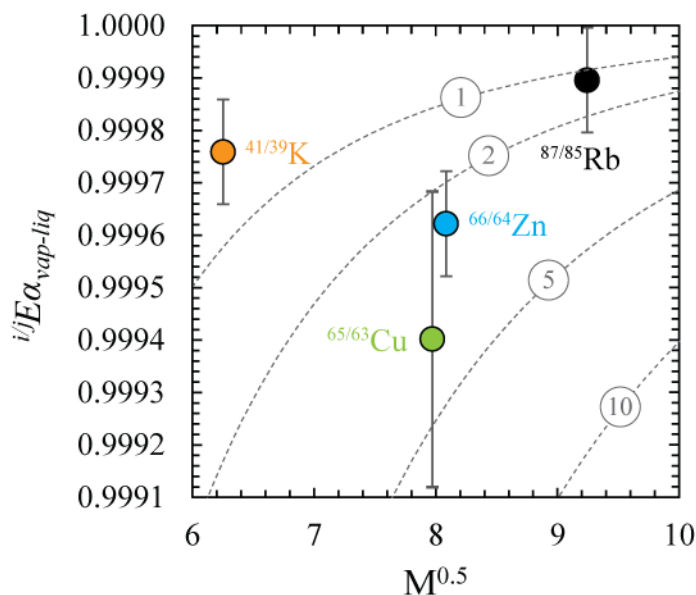
	Zn (ppm)	$\delta^{66}\text{Zn}$ (‰)	Cu (ppm)	$\delta^{65}\text{Cu}$ (‰)	K (ppm)	$\delta^{41}\text{K}$ (‰)	Rb (ppm)	$\delta^{87}\text{Rb}$ (‰)
Moon's mantle	2.1 ± 1	1.4 ± 0.2	11	0.68 ± 0.17	42 ± 6	-0.07 ± 0.09	0.125 ± 0.005	0.04 ± 0.09
Earth's mantle	53.5 ± 3	0.16 ± 0.06	30 ± 6	0.06 ± 0.10	260 ± 39	-0.48 ± 0.03	0.605 ± 0.060	-0.13 ± 0.06
$\ln f(\text{E})_{\text{Moon}}$	-3.24 ± 0.39		-1.00 ± 0.22		-1.82 ± 0.28		-1.58 ± 0.13	
$\Delta^i\text{E}_{\text{Moon-Earth}}$	1.24 ± 0.21		0.61 ± 0.20		0.41 ± 0.09		0.17 ± 0.11	
$^{i/j}\text{E}(\alpha_{\text{vap-Moon}})$	0.9996 ± 0.0001		0.9994 ± 0.0003		0.9998 ± 0.0001		0.9999 ± 0.0001	

Palme and O'Neill (2014) – Zn, K, Rb abundances BSE; Wang and Becker (2015) – Cu abundances BSE; Taylor and Wieczorek (2014), O'Neill (1991) – Zn, K, Rb abundances Moon; Ni et al. (2019) – Zn, Cu, K abundances Moon; Paniello et al. (2012), Kato et al. (2015) – $\delta^{66}\text{Zn}_{\text{Moon}}$; Sossi et al., (2018) – $\delta^{66}\text{Zn}_{\text{Earth}}$; Herzog et al. 2009, Day et al. (2019) – $\delta^{65}\text{Cu}_{\text{Moon}}$; Liu et al. (2015) – $\delta^{65}\text{Cu}_{\text{Earth}}$; Wang and Jacobsen (2016), Tian et al. (2020) – $\delta^{41}\text{K}_{\text{Earth, Moon}}$; Pringle and Moynier (2017), Nie and Dauphas (2019) – $\delta^{87}\text{Rb}_{\text{Earth, Moon}}$.

812

813 In each case, the calculated $^{i/j}\text{E}(\alpha_{\text{vap-liq}})$ lies between 0.9994 ± 0.0002 (Cu) and 0.9999 ± 0.0001 (Rb).
814 The diffusion-limited fractionation factor approaches these values only for an H_2 -rich gas with mean
815 molar mass ~ 2 g/mol (Fig. 10). However, such a scenario is doubtful considering that *i*) the strong
816 temperature contrast in the proto-lunar atmosphere that would have promoted convection preventing
817 the establishment of a diffusive gradient (Thompson and Stevenson, 1988), *ii*) a hydrogen-rich
818 atmosphere likely never existed in the protolunar disk or early Moon due to the propensity for
819 hydrodynamic escape to occur in its early evolution in the vicinity of the Earth's Roche Limit (Nakajima
820 and Stevenson, 2018; Charnoz et al., 2019), *iii*) it is not clear whether the Moon's atmosphere was ever
821 thick enough to produce total pressures that would cause evaporative loss to be diffusion-limited. Even
822 had the Moon retained most of its hydrogen, at any reasonable oxygen fugacity in an atmosphere in
823 equilibrium with silicate material, between the IW and FMQ buffers (Visscher and Fegley, 2013), the
824 $\text{H}_2/\text{H}_2\text{O}$ ratio varies between 0.5 and 0.02, respectively, such that the mean molecular mass of the gas
825 was likely to be >10 g/mol. Figure 10 was constructed presuming that each element vaporised as a
826 monatomic gas (*e.g.* Cu^0 , Zn^0). However, in volcanic gases, Cu, Zn and the alkali metals tend to form
827 chloride species (Symonds and Reed, 1993; Churakov et al., 2000; Renggli et al., 2017; Henley and
828 Seward, 2018). Nevertheless, Sossi and Fegley (2018) showed that, for a steam atmosphere produced
829 by evaporation of the bulk silicate Earth at 2000 K, $\text{ZnCl}_2(\text{g})$ and $\text{CuCl}(\text{g})$ form only at pressures $\gg 1$

830 bar, suggesting they were unlikely to have been present in the more tenuous atmosphere of the proto-
 831 Moon at magmatic temperatures (> 1000 °C).



832
 833 **Figure 11.** Best estimates for the isotopic fractionation factor of four well-defined moderately volatile elements
 834 between the Earth’s mantle and the Moon’s mantle against the square root of their mean molar masses. Overlain
 835 on the lunar data are grey dashed curves showing the fractionation that would arise during diffusion-limited
 836 evaporation into fictive atmospheres with different mean molar masses in g/mol (numbers in circles).

837 That these metals were likely present as monatomic gases suggests that, should transport phenomena
 838 have been important in causing isotopic fractionation, a correlation would be expected with molecular
 839 mass, the predominant variable controlling diffusion rates in condensed phases and gases. Figure 11
 840 illustrates that this is not observed, strongly arguing against any kind of non-equilibrium process in
 841 setting the relative isotopic fractionations among MVEs. Fractionation factors shown in Table 3 also
 842 overlap with those calculated by *ab-initio* models, for which equilibrium values of $i/jE(\alpha_{vap-liq})$ between
 843 common silicate minerals and monatomic gas range from ~ 0.9995 at 1000 K to ~ 0.9999 at 2000 K for
 844 K, Zn and Rb (Ducher et al. 2016; Li et al. 2019; Zeng et al. 2019), though the relevance of these
 845 mineral-gas fractionation factors to Moon-forming conditions remains uncertain. That equilibrium
 846 partial pressures more strongly influence lunar volatile depletion than do mass transport phenomena is
 847 also supported by the scaling of lunar element depletion factors with chemical affinity (*e.g.* O’Neill,
 848 1991). The alkali metals evaporate according to a similar stoichiometry; where $M^+O_{0.5} (l, s) = M^0(g) +$
 849 $\frac{1}{2}O_2$ (barring Cs, for which $Cs_2O(g)$ is an abundant gas species; Sossi and Fegley, 2018), and are each
 850 conspicuously depleted to a similar extent in the Moon relative to Earth’s mantle (a factor of 6, save for
 851 Li which is non-volatile). This commonality comes despite large differences in molar masses (Δm_{Rb-Na}
 852 $= 55.5$ g/mol) that far exceed any small differences in isotopic mass ($\Delta m_{41K-39K} = 2$ g/mol), a property
 853 that would engender elemental separation by mass transport in a gas phase (*section 4.2.*). A chemical
 854 equilibrium control on volatile element fractionation on the Moon is also supported by dynamical
 855 models of planetesimal atmospheres which suggest that equilibrium is readily attained, even at low total
 856 pressures (Young et al. 2019), and the lighter isotope compositions of Cr and Sn in the Moon (Sossi et
 857 al., 2018; Wang et al., 2019) relative to Earth’s mantle, which would be violated by any mass-transport
 858 process that favours loss of the lighter isotope.

859 Conversely, H_2 -rich gases may be instrumental in dampening isotopic fractionation in primary planetary
 860 atmospheres that evolved by accretion of nebular gas. These high-pressure, hydrogen-rich environments
 861 likely characterised accretion zones of chondrites and of the terrestrial planets < 5 Myr, the approximate
 862 timing of loss of the nebular gas to the Sun (Dauphas and Chaussidon, 2011). This phenomenon may

863 also explain why isotopic fractionation attending chondrule formation is limited in the solar nebula (*e.g.*
864 Alexander et al., 2000; Galy et al., 2000; Pringle et al., 2017), where H₂ is by far the dominant
865 constituent. Alternatively, when evaporation becomes so fast relative to the diffusion rate that t_{diff}/t_{evap}
866 tends to infinity, $^{i/j}E(\alpha_{vap-liq})_{net}$ tends to unity, which means that evaporation can occur without any
867 isotopic fractionation provided the diffusion rate in the condensed phase is very low and/or the
868 evaporation rate is very fast. These conditions may typify the evaporation of dry, siliceous silicate melts
869 or sublimation of solids in the reducing nebular gas (see also Ozawa and Nagahara, 2001). Such H-rich
870 conditions may also be expected to be present on hot, close-in exoplanets with escaping steady-state
871 atmospheres (Owen, 2019), and may serve to understand isotope ratios of volatile elements heavier than
872 hydrogen.

873

874 6.0. Conclusions

875 We establish that isotopic fractionation during evaporation of Cu and Zn from basaltic silicate melts at
876 1 bar, for which evaporation is not limited by diffusion in the melt, follows $^{66/64}\text{Zn}(\alpha_{\text{vap-liq}}) = 0.9959 \pm$
877 0.0002 and $^{65/63}\text{Cu}(\alpha_{\text{vap-liq}}) = 0.9972 \pm 0.0001$. Fractionation factors become closer to unity for lower
878 oxygen fugacity, as the vaporisation rate increases, despite no change in vaporisation reaction
879 stoichiometries. These experiments are zoned, and we derive diffusion rates for Cu and Zn in ferrobasalt
880 at 1300 °C (2.61×10^{-9} m²/s and $1.56 \pm 0.25 \times 10^{-9}$ m²/s, respectively), that remain constant with $f\text{O}_2$.
881 Thus, the ratio of the timescale of evaporation/diffusion decreases such that a heavy-isotope rich
882 boundary layer develops at the evaporating surface of the melt at lower $f\text{O}_2$. This occurs because, even
883 though the diffusion of the lighter isotope is faster than the heavier isotope by a factor $(M_j/M_i)^\beta$, this
884 factor, in which $\beta \approx 0.015$, is closer to 1 than is the vapour-liquid fractionation factor at the surface. The
885 net fractionation factor is therefore also closer to unity in cases where diffusion in the liquid is slower
886 than evaporation, and, at the extreme, results in no isotopic fractionation for infinitesimally slow
887 diffusion rates.

888 We develop a new formalism describing transport of the evaporating species in the gas phase, which
889 dictates its ability to escape from the evaporating surface. For natural convection in the gas at 1 bar, the
890 partial pressure of the evaporating species at the surface in a steady state is ~99% of that of its
891 equilibrium partial pressure. Under these conditions, we show that mass loss is limited according to the
892 diffusion rate of species i through the gas of mean molar mass k to the power of $2/3$, which is itself
893 proportional to the inverse square-root of their reduced mass, $\mu_{ik}^{-1/2}$. Isotopic fractionation between two
894 isotopes i and j , is therefore proportional to $(\mu_{jk}/\mu_{ik})^{1/3}$. This formalism reproduces the fractionation factor
895 of the isotopes of K, Cu and Zn in experiments of silicate melt evaporation at 1 bar in different gas
896 mixtures to within $^{i/j}\text{E}(\alpha_{\text{vap-liq}}) \pm 0.0005$. As the fractionation factor depends on the reduced mass, it is
897 sensitive to not only the mass of the evaporating species, but also to that of the atmosphere into which
898 it evaporates, with heavier atmospheres promoting fractionation.

899 Provided that the evaporation of tektites occurs in air and at 1 bar, the isotopic fractionation recorded
900 in Cu and Zn in these impact glasses overlaps with those predicted by our model, $^{i/(i-2)}\text{E}(\alpha_{\text{vap-liq}}) = 0.9966$.
901 Contrastingly, the isotopic fractionation factors of semi-volatile metals for vapour loss from the Moon,
902 as inferred from the composition of lunar mare basalts, are much closer to unity than predicted, save for
903 if vaporisation occurred into a pure H₂ atmosphere. However, the fact that such atmospheric
904 compositions are unlikely to have been stable on the early Moon, together with a lack of a strong mass
905 dependence among the depletion of alkali metals or their isotopes, suggest that mass transport was not
906 an important process in causing isotopic fractionation on the Moon.

907

908 Acknowledgements

909 PAS thanks the Swiss National Science Foundation Ambizione Fellowship (#180025). FM thanks the European
910 Research Council under the H2020 scheme with the grant #637503 (PRISTINE) and the ANR through the LABEX
911 UnivEarth. We are grateful to the Executive Editor Jeff Catalano and to Associate Editor Fang Huang for
912 exemplary editorial handling, and to Frank Wombacher, Jian Huang and Kun Wang for their comprehensive,
913 thorough and constructive reviews that made for a more accessible and carefully-considered article. We appreciate
914 the assistance of Michel Fialin and Nicolas Rividi on the Microprobe, and Marcel Guillong and Pete Tollan on
915 the Laser. We thank Mike Jollands for an introduction to finite difference modelling.

916

917 **References**

- 918 Ackermann R. J., Thorn R. J. and Winslow G. H. (1962) *Some fundamental aspects of vaporization*,
 919 Argonne National Laboratory, Illinois.
- 920 Alexander C. M. O., Grossman J. N., Wang J., Zanda B., Bourot-Denise M. and Hewins R. H. (2000)
 921 The lack of potassium-isotopic fractionation in Bishunpur chondrules. *Meteorit. Planet. Sci.* **35**,
 922 859–868.
- 923 Bartlett R. W. (1967) Platinum Oxidation Kinetics with Convective Diffusion and Surface Reaction.
 924 *J. Electrochem. Soc.* **114**, 547–550.
- 925 Borisov A. A. (2009) Influence of SiO₂ and Al₂O₃ on the activity coefficients of alkalis in melts: an
 926 experimental study. *Petrology* **17**, 579.
- 927 Boss A. P. (1998) Temperatures in protoplanetary disks. *Annu. Rev. Earth Planet. Sci.* **26**, 53–80.
- 928 Boyce J. W., Kanee S. A., McCubbin F. M., Barnes J. J., Bricker H. and Treiman A. H. (2018) Early
 929 loss, fractionation, and redistribution of chlorine in the Moon as revealed by the low-Ti lunar
 930 mare basalt suite. *Earth Planet. Sci. Lett.* **500**, 205–214.
- 931 BVSP (1981) *Basaltic Volcanism Study Project*, Pergamon Press Inc., New York.
- 932 Canup R. M., Visscher C., Salmon J. and Fegley B. (2015) Lunar volatile depletion due to incomplete
 933 accretion within an impact-generated disk. *Nat. Geosci.*, **8**, 918–921.
- 934 Chapman S. and Cowling T. G. (1970) *The Mathematical Theory of Non-Uniform Gases*. 3rd ed.,
 935 Cambridge University Press, Cambridge.
- 936 Charnoz S., Lee Y.-N., Sossi P. A., Allibert L., Siebert J., Hyodo R., Genda H. and Moynier F. (2019)
 937 Efficient early Moon devolatilisation just after its formation, through tidally-assisted
 938 hydrodynamic escape. In *50th Lunar and Planetary Science Conference* p. 2132.
- 939 Chilton T. H. and Colburn A. P. (1934) Mass Transfer (Absorption) Coefficients - Prediction from
 940 Data on Heat Transfer and Fluid Friction. *Ind. Eng. Chem.* **26**, 1183–1187.
- 941 Churakov S. V., Tkachenko S. I., Korzhinskii M. A., Bocharnikov R. E. and Schmulovich K. I. (2000)
 942 Evolution of composition of high temperature fumarolic gasses from Kudryavy volcano, Iturup,
 943 Kuril Islands: the thermodynamic modeling. *Geochemistry Int.* **38**, 436–451.
- 944 Craig H. (1968) Isotope separation by carrier diffusion. *Science* **159**, 93–96.
- 945 Crank J. (1975) *The mathematics of diffusion*, Clarendon Press, Oxford, UK.
- 946 Creech J. B., Moynier F. and Koeberl C. (2019) Volatile loss under a diffusion-limited regime in
 947 tektites: Evidence from tin stable isotopes. *Chem. Geol.* **528**, 119279.
- 948 Cussler E. L. (2009) *Diffusion: Mass Transfer in Fluid Systems*, Cambridge University Press,
 949 Cambridge, UK.
- 950 Dauphas N. and Chaussidon M. (2011) A Perspective from Extinct Radionuclides on a Young Stellar
 951 Object: The Sun and Its Accretion Disk. *Annu. Rev. Earth Planet. Sci.* **39**, 351–386.
- 952 Dauphas N., Janney P. E., Mendybaev R. A., Wadhwa M., Richter F. M., Davis A. M., van Zuilen M.,
 953 Hines R. and Foley C. N. (2004) Chromatographic separation and multicollection-ICP-MS
 954 analysis of iron. Investigating mass-dependent and -independent isotope effects. *Anal. Chem.* **76**,
 955 5855–63.
- 956 Davis A. M., Hashimoto A., Clayton, R. N. and Mayeda T. K. (1990) Isotope mass fractionation
 957 during evaporation of Mg₂SiO₄. *Nature* **347**, 655–658.
- 958 Day J. M. D., Kooten E. M. M. E. Van, Hofmann B. A. and Moynier F. (2020) Mare basalt meteorites

- 959 , magnesian-suite rocks and KREEP reveal loss of zinc during and after lunar formation. *Earth*
960 *Planet. Sci. Lett.* **531**, 115998.
- 961 Day J. M. D. and Moynier F. (2014) Evaporative fractionation of volatile stable isotopes and their
962 bearing on the origin of the Moon. *Philos. Trans. R. Soc. A Math. Phys. Eng. Sci.* **372**, 1–26.
- 963 Day J. M. D., Moynier F., Meshik A. P., Pradivtseva O. V and Petit D. R. (2017) Evaporative
964 fractionation of zinc during the first nuclear detonation. *Sci. Adv.* **3**, e1602668.
- 965 Day J. M. D., Sossi P. A., Shearer C. K. and Moynier F. (2019) Volatile distributions in and on the
966 Moon revealed by Cu and Fe isotopes in the “ Rusty Rock ” 66095. *Geochim. Cosmochim. Acta*
967 **266**, 131–143.
- 968 Dixon J. E., Stolper E. M. and Holloway J. R. (1995) An Experimental Study of Water and Carbon
969 Dioxide Solubilities in Mid-Ocean Ridge Basaltic Liquids. Part I: Calibrations and Solubility
970 Models. *J. Petrol.* **36**, 1607–1631.
- 971 Ducher M., Blanchard M. and Balan E. (2016) Equilibrium zinc isotope fractionation in Zn-bearing
972 minerals from first-principles calculations. *Chem. Geol.* **443**, 87–96.
- 973 Eggins S. M. and Shelley J. M. G. (2002) Compositional Heterogeneity in NIST SRM 610-617
974 Glasses. *Geostand. Geoanalytical Res.* **26**, 269–286.
- 975 Eucken A. (1913) Über das Wärmeleitvermögen, die spezifische Wärme und die innere Reibung der
976 Gase. *Phys. Z* **14**, 324–332.
- 977 Ford-Versypt A. N. and Braatz R. D. (2014) Analysis of finite difference discretization schemes for
978 diffusion in spheres with variable diffusivity. *Comput. Chem. Eng.* **71**, 241–252.
- 979 Frössling N. (1938) Über die verdunstung fallender tropfen. *Gerlands Beitr. Geophys.* **52**, 170–216.
- 980 Fuchs N. A. (1959) *Evaporation and droplet growth in gaseous media*, Pergamon Press, London.
- 981 Galy A., Young E. D., Ash R. D. and Nions R. K. O. (2000) The Formation of Chondrules at High
982 Gas Pressures in the Solar Nebula. *Science.* **290**, 1751–1754.
- 983 Giordano D., Russell J. K. and Dingwell D. B. (2008) Viscosity of magmatic liquids: A model. *Earth*
984 *Planet. Sci. Lett.* **271**, 123–134.
- 985 Guillong M., Quadt A. Von, Sakata S., Peytcheva I. and Bachmann O. (2014) LA-ICP-MS Pb – U
986 dating of young zircons from the Kos – Nisyros volcanic centre, SE Aegean arc. *J. Anal. At.*
987 *Spectrom.* **29**, 963–970.
- 988 Hashimoto A. (1990) Evaporation kinetics of forsterite and implications for the early solar nebula.
989 *Nature* **347**, 53–55.
- 990 Hauri E. H., Saal A. E., Rutherford M. J. and Van Orman J. A. (2015) Water in the moon’s interior:
991 Truth and consequences. *Earth Planet. Sci. Lett.* **409**, 252–264.
- 992 Henley R. W. and Seward T. M. (2018) Gas–solid reactions in arc volcanoes: Ancient and modern. In
993 *Reviews in Mineralogy and Geochemistry 84* (eds. P. King, B. Fegley, and T. M. Seward).
994 Mineralogical Society of America, Geochemical Society. pp. 309–349.
- 995 Herzog G. F., Moynier F., Albarède F. and Berezhnoy A. A. (2009) Isotopic and elemental
996 abundances of copper and zinc in lunar samples, Zagami, Pele’s hairs, and a terrestrial basalt.
997 *Geochim. Cosmochim. Acta* **73**, 5884–5904.
- 998 Hoenig C. L. and Searcy A. W. (1966) Knudsen and Langmuir Evaporation Studies of Stannic Oxide.
999 *J. Amer. Ceram. Soc.* **49**, 128–134.
- 1000 Holzheid A. and Lodders K. (2001) Solubility of copper in silicate melts as function of oxygen and
1001 sulfur fugacities, temperature, and silicate composition. *Geochim. Cosmochim. Acta* **65**, 1933–

- 1002 1951.
- 1003 Humayun M. and Cassen P. (2000) Processes Determining the Volatile Abundances of the Meteorites
1004 and Terrestrial Planets. In *The Origin of the Earth and Moon* (eds. R. M. Canup and K. Righter).
1005 University of Arizona Press, Tucson. pp. 3–23.
- 1006 Humayun M. and Clayton R. N. (1995) Potassium isotope cosmochemistry: Genetic implications of
1007 volatile element depletion. *Geochim. Cosmochim. Acta* **59**, 2131–2148.
- 1008 Humayun M. and Koeberl C. (2004) Potassium isotopic composition of Australasian tektites.
1009 *Meteorit. Planet. Sci.* **39**, 1509–1516.
- 1010 Janney P. E., Mendybaev R. A., Dauphas N., Davis A. M., Richter F. M. and Wadhwa M. (2004)
1011 “Nonideal” isotopic fractionation behaviour of magnesium in evaporation residues. In *Lunar and*
1012 *Planetary Science Conference XXXV* p. 2092.
- 1013 Jiang Y., Chen H., Fegley B., Lodders K., Hsu W., Jacobsen S. B. and Wang K. (2019) Implications
1014 of K, Cu and Zn isotopes for the formation of tektites. *Geochim. Cosmochim. Acta* **259**, 170–
1015 187.
- 1016 Kamber B.S. & Schoenberg R. (2020) Evaporative loss of moderately volatile metals from the
1017 superheated 1849 Ma Sudbury impact melt sheet inferred from stable Zn isotopes. *Earth Planet.*
1018 *Sci. Lett.* **544**, 116356.
- 1019 Kato C., Moynier F., Valdes M. C., Dhaliwal J. K. and Day J. M. D. (2015) Extensive volatile loss
1020 during formation and differentiation of the Moon. *Nat. Commun.* **6**, 7617.
- 1021 Knacke O. and Stranski I. N. (1952) The mechanism of evaporation. *Prog. Met. Phys.*, 181–235.
- 1022 Knight K. B., Kita N. T., Mendybaev R. A., Richter F. M., Davis A. M. and Valley J. W. (2009)
1023 Silicon isotopic fractionation of CAI-like vacuum evaporation residues. *Geochim. Cosmochim.*
1024 *Acta* **73**, 6390–6401.
- 1025 Knudsen M. (1909) Die Gesetze der Molekularströmung und der inneren Reibungsströmung der Gase
1026 durch Röhren. *Ann. Phys.* **333**, 75–130.
- 1027 Koeberl C. (1986) Geochemistry of tektites and impact glasses. *Annu. Rev. Earth Planet. Sci.* **14**,
1028 323–350.
- 1029 Koeberl C. (1994) Tektite origin by hypervelocity asteroidal or cometary impact. *Large Meteor.*
1030 *Impacts Planet. Evol.* **293**, 133.
- 1031 Lamoreaux R. H., Hildenbrand D. L. and Brewer L. (1987) High-Temperature Vaporization Behavior
1032 of Oxides II. Oxides of Be, Mg, Ca, Sr, Ba, B, Al, Ga, In, Tl, Si, Ge, Sn, Pb, Zn, Cd, and Hg. *J.*
1033 *Phys. Chem. Ref. Data* **16**, 419.
- 1034 Langmuir I. (1916) The evaporation, condensation and reflection of molecules and the mechanism of
1035 adsorption. *Phys. Rev.* **8**, 149–176.
- 1036 Li Y., Wang W., Wu Z., and Huang S. (2019) First-principles investigation of equilibrium K isotope
1037 fractionation among K-bearing minerals. *Geochim. Cosmochim. Acta*, **264**, 30–42.
- 1038 Liu S. A., Huang J., Liu J., Wörner G., Yang W., Tang Y. J., Chen Y., Tang L., Zheng J. and Li S.
1039 (2015) Copper isotopic composition of the silicate Earth. *Earth Planet. Sci. Lett.* **427**, 95–103.
- 1040 Liu T. and Bautista R. G. (1981) Prediction of the Global Volatilization Rate of Gas-Metal-Alloy
1041 Reaction Systems-Method of Calculation. *Oxid. Met.* **16**, 243–252.
- 1042 Lock S. J., Stewart S. T., Petaev M. I., Leinhardt Z., Mace M. T., Jacobsen S. B., and Cuk M. (2018)
1043 The origin of the Moon within a terrestrial synestia. *J. Geophys. Res.: Planets* **123**, 910–951
- 1044 Lowry R. K., Henderson P. and Nolan J. (1982) Tracer diffusion of some alkali, alkaline-earth and

- 1045 transition element ions in a basaltic and an andesitic melt, and the implications concerning melt
1046 structure. *Contrib. to Mineral. Petrol.* **80**, 254–261.
- 1047 Luck J.-M., Othman D. Ben and Albarède F. (2005) Zn and Cu isotopic variations in chondrites and
1048 iron meteorites: Early solar nebula reservoirs and parent-body processes. *Geochim. Cosmochim.*
1049 *Acta* **69**, 5351–5363.
- 1050 Mason E. A. (1957) Higher Approximations for the Transport Properties of Binary Gas Mixtures. II.
1051 Applications. *J. Chem. Phys.* **27**, 782–790.
- 1052 Melosh H. J. and Vickery A. M. (1991) Melt droplet formation in energetic impact events. *Nature*
1053 **350**, 494 – 497.
- 1054 Mendybaev R. A., Williams C. D., Spicuzza M. J., Richter F. M., Valley J. W., Fedkin A. V and
1055 Wadhwa M. (2017) Thermal and chemical evolution in the early Solar System as recorded by
1056 FUN CAIs : Part II – Laboratory evaporation of potential CMS-1 precursor material. *Geochim.*
1057 *Cosmochim. Acta* **201**, 49–64.
- 1058 Moynier F., Albarède F. and Herzog G. F. (2006) Isotopic composition of zinc, copper, and iron in
1059 lunar samples. *Geochim. Cosmochim. Acta* **70**, 6103–6117.
- 1060 Moynier F., Beck P., Jourdan F., Yin Q. Z., Reimold U. and Koeberl C. (2009) Isotopic fractionation
1061 of zinc in tektites. *Earth Planet. Sci. Lett.* **277**, 482–489.
- 1062 Moynier F., Koeberl C., Beck P., Jourdan F. and Telouk P. (2010) Isotopic fractionation of Cu in
1063 tektites. *Geochim. Cosmochim. Acta* **74**, 799–807.
- 1064 Mungall J. E. (2002) Empirical models relating viscosity and tracer diffusion in magmatic silicate
1065 melts. *Geochim. Cosmochim. Acta* **66**, 125–143.
- 1066 Nakajima M. and Stevenson D. J. (2018) Inefficient volatile loss from the Moon-forming disk:
1067 Reconciling the giant impact hypothesis and a wet Moon. *Earth Planet. Sci. Lett.* **487**, 117–126.
- 1068 Ni P. and Zhang Y. (2016) Cu diffusion in a basaltic melt. *Am. Mineral.* **101**, 1474–1482.
- 1069 Ni P., Zhang Y., Chen S. and Gagnon J. (2019) A melt inclusion study on volatile abundances in the
1070 lunar mantle. *Geochim. Cosmochim. Acta* **249**, 17–41.
- 1071 Nie N. X. and Dauphas N. (2019) Vapor Drainage in the Protolunar Disk as the Cause for the
1072 Depletion in Volatile Elements of the Moon. *Astrophys. J. Lett.* **884**, L48.
- 1073 O'Neill H. S. C. (1991) The origin of the moon and the early history of the earth—A chemical model.
1074 Part 2: The earth. *Geochim. Cosmochim. Acta* **55**, 1159–1172.
- 1075 O'Neill H. S. C. and Eggins S. M. (2002) The effect of melt composition on trace element
1076 partitioning: an experimental investigation of the activity coefficients of FeO, NiO, CoO, MoO₂
1077 and MoO₃ in silicate melts. *Chem. Geol.* **186**, 151–181.
- 1078 Owen J. E. (2019) Atmospheric Escape and the Evolution of Close-in Exoplanets. *Annu. Rev. Earth*
1079 *Planet. Sci.* **47**, 67–90.
- 1080 Ozawa K. and Nagahara H. (2001) Chemical and isotopic fractionations by evaporation and their
1081 cosmochemical implications. *Geochim. Cosmochim. Acta* **65**, 2171–2199.
- 1082 Palme H., Larimer J. W. and Lipschutz M. E. (1988) Moderately Volatile Elements. In *Meteorites and*
1083 *the Early Solar System* (eds. J. F. Kerridge and M. S. Matthews). University of Arizona Press,
1084 Tucson, pp. 436–461.
- 1085 Palme H. and O'Neill H. S. C. (2014) Cosmochemical Estimates of Mantle Composition. In *Treatise*
1086 *on Geochemistry, Vol. 3: The Mantle and Core* (ed. R. W. Carlson). Elsevier B.V., Amsterdam.
1087 pp. 1–39.

- 1088 Paniello R. C., Day J. M. D. and Moynier F. (2012) Zinc isotopic evidence for the origin of the Moon.
1089 *Nature* **490**, 376–9.
- 1090 Penner S. S. (1952) On the Kinetics of Evaporation. *J. Phys. Chem.* **56**, 475–479.
- 1091 Poitrasson F., Halliday A. N., Lee D.-C., Levasseur S. and Teutsch N. (2004) Iron isotope differences
1092 between Earth, Moon, Mars and Vesta as possible records of contrasted accretion mechanisms.
1093 *Earth Planet. Sci. Lett.* **223**, 253–266.
- 1094 Pringle E. A. and Moynier F. (2017) Rubidium isotopic composition of the Earth, meteorites, and the
1095 Moon: Evidence for the origin of volatile loss during planetary accretion. *Earth Planet. Sci. Lett.*
1096 **473**, 62–70.
- 1097 Pringle E. A., Moynier F., Beck P., Paniello R. and Hezel D. C. (2017) The origin of volatile element
1098 depletion in early solar system material: Clues from Zn isotopes in chondrules. *Earth Planet.*
1099 *Sci. Lett.* **468**, 62–71.
- 1100 Ranz W. E. and Marshall, W. R. (1952) Evaporation from Drops. Part I. *Chem. Eng. Prog.* **48**, 141–
1101 146.
- 1102 Rappé A. K., Casewit C. J., Colwell K. S., Goddard W. A. and Skiff W. M. (1992) UFF, a full
1103 periodic table force field for molecular mechanics and molecular dynamics simulations. *J. Am.*
1104 *Chem. Soc.* **114**, 10024–10035.
- 1105 Renggli C. J., King P. L., Henley R. W. and Norman M. D. (2017) Volcanic gas composition, metal
1106 dispersion and deposition during explosive volcanic eruptions on the Moon. *Geochim.*
1107 *Cosmochim. Acta* **206**, 296–311.
- 1108 Richter F. M. (2004) Timescales determining the degree of kinetic isotope fractionation by
1109 evaporation and condensation. *Geochim. Cosmochim. Acta* **68**, 4971–4992.
- 1110 Richter F. M., Dauphas N. and Teng F.-Z. (2009) Non-traditional fractionation of non-traditional
1111 isotopes: Evaporation, chemical diffusion and Soret diffusion. *Chem. Geol.* **258**, 92–103.
- 1112 Richter F. M., Davis A. M., Ebel D. S. and Hashimoto A. (2002) Elemental and isotopic fractionation
1113 of type B calcium-, aluminum-rich inclusions: Experiments, theoretical considerations, and
1114 constraints on their thermal evolution. *Geochim. Cosmochim. Acta* **66**, 521–540.
- 1115 Richter F. M., Janney P. E., Mendybaev R. A., Davis A. M. and Wadhwa M. (2007) Elemental and
1116 isotopic fractionation of Type B CAI-like liquids by evaporation. *Geochim. Cosmochim. Acta*
1117 **71**, 5544–5564.
- 1118 Richter F. M., Mendybaev R. A., Christensen J. N., Ebel D. and Gaffney A. (2011) Laboratory
1119 experiments bearing on the origin and evolution of olivine-rich chondrules. *Meteorit. Planet.*
1120 *Sci.* **46**, 1152–1178.
- 1121 Rodovská Z., Magna T., Žák K., Kato C., Savage P. S., Moynier F., Skála R. and Jezek J. (2017)
1122 Implications for behavior of volatile elements during impacts — Zinc and copper systematics in
1123 sediments from the Ries impact structure and central European tektites. *Meteorit. Planet. Sci.* **52**,
1124 2178–2192.
- 1125 Rudnick R. L. and Gao S. (2003) Composition of the Continental Crust. In *Treatise on Geochemistry*
1126 *Vol. 3* (ed. R. L. Rudnick). Elsevier, Amsterdam. pp. 1–64.
- 1127 Schneider D. A., Kent D. V and Mello G. A. (1992) A detailed chronology of the Australasian impact
1128 event, the Brunhes-Matuyama geomagnetic polarity reversal, and global climate change. *Earth*
1129 *Planet. Sci. Lett.* **111**, 395–405.
- 1130 Sedaghatpour F. and Jacobsen S. B. (2019) Magnesium stable isotopes support the lunar magma
1131 ocean cumulate remelting model for mare basalts. *Proc. Natl. Acad. Sci.* **116**, 73–78.

- 1132 Sharp Z. D., Shearer C. K., McKeegan K. D., Barnes J. D. and Wang Y. Q. (2010) The chlorine
1133 isotope composition of the moon and implications for an anhydrous mantle. *Science*. **329**, 1050–
1134 1053.
- 1135 Shearer C. K., Elardo S. M., Petro N. E., Borg L. E. and McCubin F. M. (2015) Origin of the lunar
1136 highlands Mg-suite: An integrated petrology, geochemistry, chronology, and remote sensing
1137 perspective. *Am. Mineral.* **100**, 294–325.
- 1138 Shornikov S. I. (2015) Vaporization coefficients of oxides contained in the melts of Ca-Al-inclusions
1139 in chondrites. *Geochemistry Int.* **53**, 1080–1089.
- 1140 Sossi P. A. and Fegley B. (2018) Thermodynamics of Element Volatility and its Application to
1141 Planetary Processes. In *Reviews in Mineralogy and Geochemistry 84: High temperature gas-
1142 solid reactions in Earth and planetary processes* (eds. P. L. King, T. M. Seward, and B. Fegley).
1143 Mineralogical Society of America, Chantilly. pp. 393–459.
- 1144 Sossi P. A., Halverson G. P., Nebel O. and Eggins S. M. (2015) Combined Separation of Cu, Fe and
1145 Zn from Rock Matrices and Improved Analytical Protocols for Stable Isotope Determination.
1146 *Geostand. Geoanalytical Res.* **39**, 129–149.
- 1147 Sossi P. A., Klemme S., O'Neill H. S. C., Berndt J. and Moynier F. (2019) Evaporation of moderately
1148 volatile elements from silicate melts: experiments and theory. *Geochim. Cosmochim. Acta* **260**,
1149 204–231.
- 1150 Sossi P. A. and Moynier F. (2017) Chemical and isotopic kinship of iron in the Earth and Moon
1151 deduced from the lunar Mg-Suite. *Earth Planet. Sci. Lett.* **471**, 125–135.
- 1152 Sossi P. A., Moynier F. and van Zuilen K. (2018) Volatile loss following cooling and accretion of the
1153 Moon revealed by chromium isotopes. *Proc. Natl. Acad. Sci.* **115**, 10920–10925.
- 1154 Sossi P. A., Nebel O., O'Neill H. S. C. and Moynier F. (2018) Zinc isotope composition of the Earth
1155 and its behaviour during planetary accretion. *Chem. Geol.* **477**, 73–84.
- 1156 Stevenson R. J., Bagdassarov N. S., Dingwell D. B. and Romano C. (1998) The influence of trace
1157 amounts of water on the viscosity of rhyolites. *Bull. Volcanol.* **60**, 89–97.
- 1158 Symonds R. B. and Reed M. H. (1993) Calculation of Multicomponent chemical equilibria in gas-
1159 solid-liquid systems: Calculation methods, thermochemical data, and applications to studies of
1160 high-temperature volcanic gases with examples from Mount St. Helens. *Am. J. Sci.* **293**, 758–
1161 864.
- 1162 Taylor G. J. and Wieczorek M. A. (2014) Lunar bulk chemical composition: a post-Gravity Recovery
1163 and Interior Laboratory reassessment. *Philos. Trans. R. Soc. A Math. Phys. Eng. Sci.* **372**,
1164 20130242.
- 1165 Taylor S. R. and Kaye M. (1969) Genetic significance of the chemical composition of tektites : A
1166 review. *Geochim. Cosmochim. Acta* **33**, 1083–1100.
- 1167 Thompson C. and Stevenson D. J. (1988) Gravitational Instability in Two-Phase Disks and the Origin
1168 of the Moon. *Astrophys. J.* **333**, 452–481.
- 1169 Tian Z., Jolliff B. L., Korotev R. L., Fegley B., Lodders K., Day J. M., Chen H., and Wang K. (2020).
1170 Potassium isotopic composition of the Moon. *Geochim. Cosmochim. Acta* **280**, 263–280.
- 1171 Visscher C. and Fegley B. (2013) Chemistry of impact-generated silicate melt-vapor debris disks. *ApJ*
1172 *Lett.* **767**, L12.
- 1173 Wang J., Davis A. M., Clayton R. N., Mayeda T. K. and Hashimoto A. (2001) Chemical and isotopic
1174 fractionation during the evaporation of the FeO-MgO-SiO₂-CaO-Al₂O₃-TiO₂ rare earth element
1175 melt system. *Geochim. Cosmochim. Acta* **65**, 479–494.

- 1176 Wang K. and Jacobsen S. B. (2016) Potassium Isotopic Evidence for the Origin of the Moon. *Nature*
1177 **538**, 487–490.
- 1178 Wang X., Fitoussi C., Bourdon B., Fegley B. and Charnoz S. (2019) Tin isotopes indicative of liquid-
1179 vapour equilibration and separation in the Moon-forming disk. *Nat. Geosci.* **12**, 707–712.
- 1180 Wang Z. and Becker H. (2015) Abundances of Ag and Cu in mantle peridotites and the implications
1181 for the behavior of chalcophile elements in the mantle. *Geochim. Cosmochim. Acta* **160**, 209–
1182 226.
- 1183 Warren P. H. (2005) “New” lunar meteorites- Implications for composition of the global lunar
1184 surface, lunar crust and the bulk Moon. *Meteorit. Planet. Sci.* **40**, 477–506.
- 1185 Wimber R. T., Hills S. W., Wahl N. K. and Tempero C. R. (1977) Kinetics of Evaporation / Oxidation
1186 of Iridium. *Metall. Trans. A* **8A**, 193 – 199.
- 1187 Wimpenny J., Marks N., Knight K., Rolison J. M., Borg L., Eppich G., Badro J., Ryerson F. J.,
1188 Sanborn M., Huyskens M. H. and Yin Q. (2019) Experimental determination of Zn isotope
1189 fractionation during evaporative loss at extreme temperatures. *Geochim. Cosmochim. Acta* **259**,
1190 391–411.
- 1191 Wombacher F., Rehkämper M. and Mezger K. (2004) Determination of the mass-dependence of
1192 cadmium isotope fractionation during evaporation. *Geochim. Cosmochim. Acta* **68**, 2349–2357.
- 1193 Wombacher F., Rehkämper M., Mezger K., Bischoff A. and Münker C. (2008) Cadmium stable
1194 isotope cosmochemistry. *Geochim. Cosmochim. Acta* **72**, 646–667.
- 1195 Wombacher F., Eisenhauer A., Böhm F., Gussone N., Regenber M., Dullo W. C. and Rüggeberg A.
1196 (2011) Magnesium stable isotope fractionation in marine biogenic calcite and aragonite.
1197 *Geochim. Cosmochim. Acta* **75**, 5797–5818.
- 1198 Young E. D. (2000) Assessing the implications of K isotope cosmochemistry for evaporation in the
1199 preplanetary solar nebula. *Earth Planet. Sci. Lett.* **183**, 321–333.
- 1200 Young E. D. and Galy A. (2004) The isotope geochemistry and cosmochemistry of magnesium. *Rev.*
1201 *Mineral. Geochem.* **55**, 197–230.
- 1202 Young E. D., Kohl I. E., Warren P. H., Rubie D. C., Jacobson S. A. and Morbidelli A. (2016) Oxygen
1203 isotopic evidence for vigorous mixing during the Moon-forming giant impact. *Science* **351**, 493–
1204 496.
- 1205 Young E. D., Shahar A., Nimmo F., Schlichting H. E., Schauble E. A., Tang H. and Labidi J. (2019)
1206 Near-equilibrium isotope fractionation during planetesimal evaporation. *Icarus* **323**, 1–15.
- 1207 Yu Y., Hewins R. H., Alexander C. M. O. D. and Wang J. (2003) Experimental study of evaporation
1208 and isotopic mass fractionation of potassium in silicate melts. *Geochim. Cosmochim. Acta* **67**,
1209 773–786.
- 1210 Žák K., Skála R., Řanda Z., Mizera J., Heissig K., Ackerman L., Ďurišová J., Jonášová Š., Kameník J.
1211 and Magna T. (2016) Chemistry of tertiary sediments in the surroundings of the ries impact
1212 structure and moldavite formation revisited. *Geochim. Cosmochim. Acta* **179**, 287–311.
- 1213 Zeng H., Rozsa V. F., Nie N. X., Zhang Z., Pham T. A., Galli G. and Dauphas N. (2019). *Ab Initio*
1214 calculation of equilibrium isotopic fractionations of potassium and rubidium in minerals and
1215 water. *ACS Earth Space Chem.* **3**, 2601–2612.
- 1216 Zhang J., Dauphas N., Davis A. M., Leya I. and Fedkin A. (2012) The proto-Earth as a significant
1217 source of lunar material. *Nat. Geosci.* **5**, 251–255.
- 1218